PONTIFICIA UNIVERSIDAD CATÓLICA DE CHILE
ESCUELA DE INGENIERÍA

# TOPOLOGY OPTIMIZATION WITH OPTIMAL DESIGN SUBDOMAIN SELECTION

**MATÍAS IGNACIO SUAU SALAS**

Thesis submitted to the Office of Research and Graduate Studies
in partial fulfillment of the requirements for the degree of
Master of Science in Engineering

Advisor:
TOMÁS ZEGARD LATRACH

Santiago de Chile, (March, 2023)

PONTIFICIA UNIVERSIDAD CATÓLICA DE CHILE
ESCUELA DE INGENIERÍA

# TOPOLOGY OPTIMIZATION WITH OPTIMAL DESIGN SUBDOMAIN SELECTION

**MATÍAS IGNACIO SUAU SALAS**

Members of the Committee:
TOMÁS ZEGARD LATRACH
SERGIO GUTIÉRREZ Sergio Gutiérrez
Sergio Gutiérrez (Mar 28, 2023 08:29 ADT)
AREK MAZUREK Arek Mazurek
Arek Mazurek (Apr 2, 2023 07:12 CDT)
PATRICIO DE LA CUADRA
Patricio de la Cuadra (Mar 30, 2023 13:33 ADT)

Thesis submitted to the Office of Research and Graduate Studies in partial fulfillment of the requirements for the degree of Master of Science in Engineering

Santiago de Chile, (March, 2023)

*To my mother, for her*
*unconditional support.*

## TABLE OF CONTENTS

## LIST OF FIGURES

## ABSTRACT

Topology optimization is a technique to solve the material distribution problem. However, consideration for manufacturing constraints within the algorithm can be challenging. A type of manufacturing constraint that has not been thoroughly addressed is the ability to optimally select among a set of design subdomains. Examples of situations that may require such constraint in their design process are: the optimal location and shape of the openings in a castellated beam, the design and optimal location of a bridge pier, and the design and location of an outrigger system for a high-rise building, to name a few. This paper presents a novel formulation to address the optimal subdomain selection and design problem which is based on an extension to the well-known SIMP formulation. The proposed formulation optimally selects the design subdomains in (2D and 3D) structures, which are topology optimized in parallel with the rest of the design domain that does not belong to any subdomain.



**Keywords**: Topology optimization, structural optimization, design subdomian, multiple load cases, building outrigger.

# RESUMEN

La optimización topológica es una técnica para resolver el problema de distribución de materiales. Sin embargo, la consideración de las restricciones de fabricación dentro del algoritmo puede ser un desafío. Un tipo de restricción de fabricación que no se ha abordado a fondo es la capacidad de seleccionar de manera óptima entre un conjunto de subdominios de diseño. Ejemplos de situaciones que pueden requerir tal restricción en su proceso de diseño son: la ubicación y forma óptimas de las aberturas en una viga alveolada, el diseño y ubicación óptima de una cepa de puente, y el diseño y ubicación de un sistema de *outriggers* para un edificio de gran altura, por mencionar algunos. Este artículo presenta una formulación novedosa para abordar el problema de selección y diseño de subdominios óptimos que se basa en una extensión de la conocida formulación SIMP. La formulación propuesta selecciona de manera óptima los subdominios de diseño en estructuras (2D y 3D), las cuales son topológicamente optimizadas en paralelo con el resto del dominio de diseño que no pertenece a ningún subdominio.

**Palabras Clave**: Optimización topológica, optimización estructural, subdominio de diseño, multiples casos de carga, edificio con *outriggers* .

## 1. INTRODUCTION

A frequent design problematic in engineering is to find the optimal distribution of materials that deliver the best structural performance based on a specific performance metric. Density-based topology optimization is a computational technique to iteratively solve this optimal material distribution problem. This requires an objective function (or performance metric) that measures the fitness of a proposed design and is therefore minimized by the algorithm while subjected to a set of design constraints. The objective function is based on the structural performance of a given design (or behavior), which is typically analyzed by means of the finite element method (or FEM). There are various different topology optimization approaches to solve the material distribution problem such as: homogenization (Bendsøe & Kikuchi, 1988; Suzuki & Kikuchi, 1991), SIMP[1] (Bendsøe, 1989; Zhou & Rozvany, 1991; Mlejnek, 1992; Sigmund, 2001), level-set (Wang et al., 2003; Allaire et al., 2004), phase-field (Wang & Zhou, 2004; Gain & Paulino, 2012), ESO/BESO[2] (Xie & Steven, 1997; X. Huang & Xie, 2007), to name a few.

The SIMP (or power-law) approach assumes that the material properties within each finite element are constant and dependent on a single design variable (Bendsøe, 1989; Zhou & Rozvany, 1991; Mlejnek, 1992; Sigmund, 2001). Specifically, the elastic modulus of the $i$-th element is defined by the density $\rho_i$ to the power of a penalization parameter $p$. The problem is sensitive to the value of $p$: the case of $p = 1$ can be shown to be equivalent to the variable thickness sheet problem (Petersson, 1999) and is convex; the case of $p > 1$ is attractive since it approximates the 0–1 (void–solid) solution by penalizing the intermediate densities. The problem however, becomes non-convex for values of $p > 1$ and the optimization is prone to converge towards local minima (Bendsøe & Sigmund, 2003; Sigmund & Maute, 2013).

Real engineering problems that make use of topology optimization are often subjected to manufacturing constraints, which introduce challenges in their implementation. Pattern

[1]Solid Isotropic Material with Penalization.
[2]Evolutionary Structural Optimization and Bi-directional Evolutionary Structural Optimization.

repetition and symmetry are frequent manufacturing constraints in large-size engineering problems such as buildings (Almeida et al., 2010; Stromberg et al., 2011). Casting and milling are common manufacturing processes that require material to be added or removed along an axis, which has been addressed with the use of a Heaviside projection (Guest & Zhu, 2012). Additive manufacturing is a fabrication process that allows for (very) complicated geometries. Nonetheless, even additive manufacturing is subjected to some type of manufacturing constraint which is dependent on the specific subtype of 3D printing technology being used, introducing limitations such as: minimum feature size (Tang & Chang, 2001), manufacturable inclination angle (Leary et al., 2013), hollow solid incapability (Kumar, 2003; Melchels et al., 2010; J. Huang et al., 2020), efficient use of the "support material" used in the printing (Leary et al., 2014), to name a few. Vatanabe et al. (Vatanabe et al., 2016) developed a unified projection-based method that considers a design domain and a pseudo-density domain where results are projected using a projection function to obtain the optimal solution. This method can consider manufacturing constraints such as milling, minimum hole size, turning, casting, etc.

This work focuses on a manufacturing constraint that has not yet been addressed: to optimally choose the design subdomains. Density-based topology optimization can then be used to optimize the material layout within the selected subdomains. In addition, applied problems often include an active design subdomain that must be part of the structure, i.e., the subdomain selection does not apply to an active subdomain. Thus, a method that can optimize the active design domain, but at the same time design and choose specific subdomains is needed. Engineering projects that require a method of this kind are: the optimal location and shape of the openings in a castellated beam, the optimal location and design of a bridge pier, and the optimal location and design of an outrigger system for a high-rise building, to name a few. This manuscript presents a formulation and algorithm to solve the problem of optimal subdomain selection and optimization through the use of a modified SIMP formulation.

## 2. FORMULATION

This work considers a total of three formulations, which are progressively more complicated yet offer more user flexibility. They are all based on a the SIMP formulation, which is presented here for completion purposes.

### 2.1. SIMP formulation

The SIMP formulation (Bendsøe, 1989; Zhou & Rozvany, 1991; Mlejnek, 1992; Sigmund, 2001) using a two-field density filter (Bruns & Tortorelli, 1998; Bourdin, 2001; Sigmund & Maute, 2013) is as follows:

$$
\begin{aligned}
\min_{\mathbf{x}} \quad & J = \mathbf{u}^T \, \mathbf{K} \, \mathbf{u} \\
\text{s.t.} \quad & \textstyle\sum_{i=1}^{N} \rho_i \, v_i \leq f_0 \, v_0 \\
& E^{(i)} = E_{\text{min}} + (E_0 - E_{\text{min}}) \, \rho_i^p \\
& \boldsymbol{\rho} = \mathbf{H} \, \mathbf{x} \\
& \mathbf{K} = \mathop{\mathbf{A}}_{i=1}^{N} E^{(i)} \, \mathbf{K}_0^{(i)} \\
& 0 \leq x_i \leq 1 \qquad\qquad \forall \, i = 1 \ldots N \\
\text{with} \quad & \mathbf{K} \, \mathbf{u} = \mathbf{f}
\end{aligned}
\tag{2.1}
$$

where $J = \mathbf{u}^T \, \mathbf{K} \, \mathbf{u}$ is the objective function, which in this case is the (commonly used) compliance of the structure yet a different objective could be used, $\mathbf{u}$ are the nodal displacements, and $\mathbf{K}$ is the global stiffness matrix built from the *assembly* of all $N$ elements. In addition, the two-field SIMP algorithm defines $\mathbf{x}$ as a vector of the $N$ element-wise design variables, $\boldsymbol{\rho}$ is the vector of the $N$ element-wise (filtered) densities, and $\mathbf{H}$ is a filter matrix which applies a convolution operation over the design variables (Zegard & Paulino, 2016). This filter imposes an implicit size control over the resulting topology, which addresses the illposedness of the problem and prevents the *checkerboard* phenomenon from plaguing the solution (Díaz & Sigmund, 1995; Jog & Haber, 1996; Sigmund, 2007). The

power-law defines the elastic modulus of the $i$-th element $E^{(i)}$ where, $E_{\text{min}}$ is a very small elastic modulus associated with the Ersatz material used to represent the void phase in the topology, $E_0$ is the elastic modulus of the solid phase, $\mathbf{K}_0^{(i)}$ is the stiffness matrix of the $i$-th element calculated with an unit elastic modulus (i.e. with $E = 1$), and $p$ is the SIMP penalization parameter which prevents intermediate densities.

A volume constraint is necessary since quite often the optimal solution will use as much material as is available (the case with compliance as the objective and no material self-weight). Hence, not enforcing a volume limit for the solid phase will result on a trivial solution consisting of pure solid. The standard formulation in Equation (2.1) imposes a volume constraint through the volume fraction $f_0$, a scalar parameter in the range $0 \leq f_0 \leq 1$, with $v_0$ being the total volume of the design domain equal to $\sum_{i=1}^{N} v_i$, and $v_i$ being the volume of the $i$-th element.

The optimization problem in Equation (2.1) is based on structural analysis (mechanics of solids), which is formulated through the embedded (or nested) $\mathbf{K}\,\mathbf{u} = \mathbf{f}$ system of equations, where $\mathbf{f}$ is the nodal force vector.

The optimization problem presented in Equation (2.1) is one of many techniques used to solve the solid–void (1 or 0, respectively) problem. Most of these techniques, like SIMP, require a relaxation of the design variable allowing intermediate values between 0 and 1. In the specific case of SIMP, the solution is driven close to a 0 or 1 solution by means of the penalization parameter $p$, where experimentally it has been shown that $p = 3$ yields acceptable results. However, even with higher values of penalization the solution will still exhibit some intermediate values which often require rationalization from the user before becoming a final design. For additional details on the SIMP formulation, variations, shortcomings and uses, the reader can refer to (Sigmund, 2001; Bendsøe & Sigmund, 2003; Andreassen et al., 2011).

## 2.2. SIMP with subdomain selection

The design domain can be divided into an active domain and several design subdomains which cannot all be used in the final design. The number of subdomains that can be selected and used are defined by the user and will depend on the specific problem requirements. Within the optimization algorithm, the subdomain selection is a binary variable $\mu_j$, with values 0 or 1 for unselected and selected subdomain, respectively. However, for the same reason the design variable $x_i$ is continuous in Equation (2.1), this subdomain selection variable will be continuous. In other words, the optimization algorithm uses a subdomain selection variable $0 \leq \mu_j \leq 1$. Thus, it is essential to find a way to penalize the subdomain selection variable to force the optimization to drive $\mu_j$ towards a 0 and 1 solution. Computational experimentation proved this penalization to be far from trivial and throughout this study, three different (related and increasingly robust) formulations were developed.

The subdomain selection algorithm is based on a modified SIMP power-law, where a new penalization parameter $q$ is used to drive the subdomain selection towards 0 or 1 values. Analogous to the standard SIMP penalization, the penalization parameter $q$ becomes effective for values $q > 1$ and is user-defined. Elements that do not belong to any selectable subdomain $\Omega_j$ are subjected to the standard SIMP power-law, where no $\mu_j$

variable is involved. The resulting optimization problem is as follows:

$$
\begin{aligned}
\min_{\mathbf{x},\boldsymbol{\mu}} \quad & J = \mathbf{u}^T \mathbf{K}\, \mathbf{u} \\
\text{s.t.} \quad & \textstyle\sum_{i=1}^{N} \rho_i\, v_i \leq f_0\, v_0 \\
& \textstyle\sum_{j=1}^{N_s} \mu_j \leq N_0 \\
& E^{(i)} = E_{\text{min}} + (E_0 - E_{\text{min}})\, \rho_i^p\, \mu_j^q \quad \forall\, i \in \bigcup_{j=1}^{N_s} \Omega_j \\
& E^{(i)} = E_{\text{min}} + (E_0 - E_{\text{min}})\, \rho_i^p \qquad \forall\, i \in \Omega - \bigcup_{j=1}^{N_s} \Omega_j \\
& \boldsymbol{\rho} = \mathbf{H}\, \mathbf{x} \\
& \mathbf{K} = \mathop{\mathrm{A}}_{i=1}^{N} E^{(i)}\, \mathbf{K}_0^{(i)} \\
& 0 \leq x_i \leq 1 \qquad \forall\, i = 1 \ldots N \\
& 0 \leq \mu_j \leq 1 \qquad \forall\, j = 1 \ldots N_s \\
\text{with} \quad & \mathbf{K}\, \mathbf{u} = \mathbf{f}
\end{aligned}
\tag{2.2}
$$

where $\Omega$ is the total design subdomain including the selectable subdomains, and $\Omega_j$ is the $j$-th selectable design subdomain out of the total $N_s$ selectable subdomains. The integer $N_0$ is the user-defined maximum number of design subdomains that the final solution can utilize.

The optimization problem in Equation (2.2) does succeed in solving the problem from the mathematical point of view. However, computational experimentation poses challenges and a relatively high penalization parameter $q$ is necessary to drive the optimization algorithm towards a desirable 0 or 1 selection of subdomains. Unfortunately, this approach creates an ill-conditioned problem resulting in poor convergence and exhibiting numerical issues for relatively large problems.

The optimization problem described in Equation (2.2) requires improvement. In an effort to improve the numerical issues plaguing the method, a different approach to drive the subdomain parameter $\mu_j$ towards a 0 or 1 solution is taken: the penalization on intermediate values for $\mu_j$ is applied in the constraint associated with the maximum number of

subdomains. The resulting formulation is as follows:

$$
\begin{aligned}
\min_{\mathbf{x},\boldsymbol{\mu}} \quad & J = \mathbf{u}^T \mathbf{K}\, \mathbf{u} \\
\text{s.t.} \quad & \textstyle\sum_{i=1}^{N} \rho_i\, v_i \leq f_0\, v_0 \\
& \textstyle\sum_{j=1}^{N_s} \mu_j^{1/q} \leq N_0 \\
& E^{(i)} = E_{\text{min}} + (E_0 - E_{\text{min}})\, \rho_i^p\, \mu_j \quad \forall\, i \in \bigcup_{j=1}^{N_s} \Omega_j \\
& E^{(i)} = E_{\text{min}} + (E_0 - E_{\text{min}})\, \rho_i^p \quad \forall\, i \in \Omega - \bigcup_{j=1}^{N_s} \Omega_j \\
& \boldsymbol{\rho} = \mathbf{H}\, \mathbf{x} \\
& \mathbf{K} = \mathop{\mathrm{A}}_{i=1}^{N} E^{(i)}\, \mathbf{K}_0^{(i)} \\
& 0 \leq x_i \leq 1 \quad \forall\, i = 1 \ldots N \\
& 0 \leq \mu_j \leq 1 \quad \forall\, j = 1 \ldots N_s \\
\text{with} \quad & \mathbf{K}\, \mathbf{u} = \mathbf{f}
\end{aligned}
\tag{2.3}
$$

where the penalization parameter $q$ is now acting over the constraint that limits the number of subdomains. Like all SIMP-like penalization parameters, the penalization parameter $q$ becomes effective for values $q > 1$ and is user-defined.

The optimization problem described in Equation (2.3) alleviates the conditioning problem by shifting the penalization on the $\mu_j$ variables to the subdomain constraint. This results in a global stiffness matrix $\mathbf{K}$ with almost the same conditioning as with the standard SIMP formulation and is therefore significantly better from a numerical perspective.

### 2.3. $\varepsilon$–relaxation

The initial guess of $\mu_j$ in the iterative optimization procedure will often be taken as:

$$\boldsymbol{\mu} = \frac{N_0}{N_s}\, \mathbf{1}$$

where $\mathbf{1}$ is a vector of ones. As an example, if there are 7 subdomains to choose from and only 2 can be active in the final solution, the initial guess on the subdomain selection

variables will be $\mu_j = 2/7$. This initial guess could be problematic since the penalized constraint $\sum_{j=1}^{N_s} \mu_j^{1/q} \leq N_0$ in the formulation of Equation (2.3) will be violated for any $q > 1$. This (violated) constraint will trigger a response from the optimizer. Computational experimentation has shown that this (somewhat aggressive) optimizer response can make the optimization unstable in some tests.

Alternatively, the initial value could be taken as:

$$\boldsymbol{\mu} = \left(\frac{N_0}{N_s}\right)^q \mathbf{1}$$

This value would not trigger a violated-constraint response from the optimizer, but would cause the subdomains to begin from a very low effective stiffness which may cause difficulties selecting the design subdomains, hence yielding similar problems.

Relaxing the subdomain constraint in the initial stages of the optimization gives the optimizer more freedom to choose among the available optimal subdomains early in the optimization process. For that purpose, an $\varepsilon$–relaxation approach was implemented in the constraint (Stolpe & Svanberg, 2001). This results in:

$$\sum_{j=1}^{N_s} \mu_j^{1/q} \leq N_0 \left(1 + \varepsilon\right) \tag{2.4}$$

where $\varepsilon \geq 0$ is the constraint relaxation parameter. The $\varepsilon$ value is progressively decreased throughout the optimization process until the original subdomain constraint is enforced. It should be noted that, as it was implied before, the $\varepsilon$–relaxation is not always necessary to ensure good convergence.

### 2.4. Volume fraction constraints

The volume constraint is an upper limit on the solid phase volume fraction which is often defined as $f$. This work considers three different volume constraints that the user might need to employ for the specific problem at hand:

(i) Volume constraint over all $N$ finite elements in the domain:

$$\sum_{i=1}^{N} \rho_i \, v_i \leq f_0 \, v_0 \qquad \forall \; i \in \Omega$$

(ii) Volume constraint over the $N_1$ finite elements that do not belong to any subdomain:

$$\sum_{i=1}^{N_1} \rho_i \, v_i \leq f_1 \, v_1 \qquad \forall \; i \in \Omega - \bigcup_{j=1}^{N_s} \Omega_j$$

(iii) Volume constraint over the $N_2$ finite elements that belong to the subdomains:

$$\sum_{i=1}^{N_2} \rho_i \, v_i \leq f_2 \, v_2 \qquad \forall \; i \in \bigcup_{j=1}^{N_s} \Omega_j$$

where $f_0$, $f_1$, and $f_2$ are the (scalar) volume fractions in the range $0 \ldots 1$, and $v_0$, $v_1$, and $v_2$, are the domain volumes associated with the complete domain, the domain minus the subdomains, and the subdomains, respectively. In addition, the number of finite elements satisfies $N_1 + N_2 = N$ and the volumes also satisfy $v_1 + v_2 = v_0$.

The volume constraint can all simultaneously be considered in the optimization, yet there is no guarantee that they will all be active at the optimum. Any volume constraint can be deactivated for a specific optimization problem by specifying $f = 1$ on them.

## 2.5. Final subdomain selection formulation

Considering all the previous discussions the final optimization formulation for *density-based topology optimization with design subdomain selection* is:

$$
\begin{aligned}
\min_{\mathbf{x},\boldsymbol{\mu}} \quad & J = \mathbf{u}^T \, \mathbf{K} \, \mathbf{u} \\
\text{s.t.} \quad & \textstyle\sum_{i=1}^{N} \rho_i \, v_i \leq f_0 \, v_0 && \forall \, i \in \Omega \\
& \textstyle\sum_{i=1}^{N_1} \rho_i \, v_i \leq f_1 \, v_1 && \forall \, i \in \Omega - \bigcup_{j=1}^{N_s} \Omega_j \\
& \textstyle\sum_{i=1}^{N_2} \rho_i \, v_i \leq f_2 \, v_2 && \forall \, i \in \bigcup_{j=1}^{N_s} \Omega_j \\
& \textstyle\sum_{j=1}^{N_s} \mu_j^{1/q} \leq N_0 \, (1 + \varepsilon) \\
& E^{(i)} = E_{\text{min}} + (E_0 - E_{\text{min}}) \, \rho_i^p \, \mu_j && \forall \, i \in \bigcup_{j=1}^{N_s} \Omega_j \\
& E^{(i)} = E_{\text{min}} + (E_0 - E_{\text{min}}) \, \rho_i^p && \forall \, i \in \Omega - \bigcup_{j=1}^{N_s} \Omega_j \\
& \boldsymbol{\rho} = \mathbf{H} \, \mathbf{x} \\
& \mathbf{K} = \mathop{\mathrm{A}}_{i=1}^{N} E^{(i)} \, \mathbf{K}_0^{(i)} \\
& 0 \leq x_i \leq 1 && \forall \, i = 1 \ldots N \\
& 0 \leq \mu_j \leq 1 && \forall \, j = 1 \ldots N_s \\
\text{with} \quad & \mathbf{K} \, \mathbf{u} = \mathbf{f}
\end{aligned}
\tag{2.5}
$$

The contributions of the present work are the subdomain selection technique which is here embodied by the $\boldsymbol{\mu}$ variable, and the various volume constraints $f_0$, $f_1$, and $f_2$. The optimization problem in Equation (2.5) is a *nested* optimization problem (Christensen & Klarbring, 2009), and has multiple constraints which may or may not be active in the optimum.

## 2.6. Continuation of $p$ and $q$

The optimization problem described in Equation (2.1) is convex for a penalization value of $p = 1$ and can be shown to be equivalent to the variable thickness sheet problem (Petersson, 1999). This also applies to the optimization problem developed in this work and shown in Equation (2.5).

The optimization problem becomes non-convex for values $p > 1$ and presents multiple local minima. Numerical experimentation has shown that a continuation scheme over the penalization parameter $p$ tends to converge towards better results. The continuation scheme consists of initially optimizing for a penalization value of $p = 1$ and then slowly increase to the desired penalization value. A final penalization of $p > 3$ is desired to appropriately approximate a clean 0 or 1 solution (void or solid). The continuation scheme not only improves the optimization history but also allows to reach higher $p$ values without having numerical stability issues and avoiding convergence towards a low-performing solution (local minimums).

The newly introduced subdomain penalization parameter $q$ has a similar purpose and behavior as the parameter $p$. Thus, a continuation scheme over the scalar $q$ is also advised.

The continuation scheme for $p$ and $q$ are tweaked for each example here presented. That said, in general, the minimum value is $1.25$ and the maximum target value is $4.5$, which is approached in increments of $0.25$.

## 2.7. Passive elements

The computational implementation of the formulation allows for passive elements. Passive elements can either be passive-solid $(\rho_i = 1)$; or passive-void $(\rho_i = \rho_{min})$. Both elements give the user capabilities to appropriately model situations where parts of the structure (or voids) are known, e.g. structural slabs, building cores, to name a few.

A discussion could be made where passive-void elements are unnecessary, since a better approach would be to remove them from the analysis mesh. The passive-void capability is useful when different design options involving voids at different locations need to be explored. The passive-void elements eliminate the need to re-mesh or remove elements (and nodes) from the analysis mesh. In the examples shown in the present manuscript, only passive-solid elements are used, yet the capability for passive-void exists in the proof-of-concept implementation used here.

### 2.8. MMA optimizer

To iteratively solve this problem, we have made use of the *method of moving asymptotes* (or MMA) to optimize this problem (Svanberg, 1987). The MMA algorithm requires that certain optimization parameters be appropriately scaled for it to correctly optimize the problem. The objective function $f_0(\mathbf{x})$ should be scaled in such that $1 \leq f_0(\mathbf{x}) \leq 100$. The MMA coefficients $c_i$ should avoid "extremely large" values such as $10^{10}$. The MMA author recommends the value $c_i = 1000$ or $10000$ if all of the other parameters have been scaled correctly. In addition, if the optimal solution given by the algorithm does not make all of the "*artificial optimization variables*" $y_i = 0$, the author recommends to "*increase the corresponding values of* $c_i$ *by e.g. a factor of 100 and solve the problem again*" (Svanberg, accessed December 20, 2022).

### 2.9. Sensitivity calculation

The iterative solution scheme used is a gradient-based optimization. In order to solve Equation (2.5) we need to calculate the gradients of the objective function $J$. The sensitivity calculation for density-based topology optimization is a typical requirement for this and other methods, and the reader can refer to (Bendsøe & Sigmund, 2003; Tortorelli & Michaleris, 1994; Christensen & Klarbring, 2009) for more details on this topic. Nonetheless, for the sake of completeness and to highlight some differences of the subdomain selection formulation, the complete derivation will be presented.

Taking the derivative of $J$ with respect to $\rho_i$ and $\mu_j$ we obtain the following:

$$\frac{\mathrm{d}J}{\mathrm{d}\rho_i} = \frac{\partial J}{\partial \rho_i} + \frac{\partial J}{\partial \mathbf{u}}^T \frac{\partial \mathbf{u}}{\partial \rho_i} \tag{2.6a}$$

$$\frac{\mathrm{d}J}{\mathrm{d}\mu_j} = \frac{\partial J}{\partial \mu_j} + \frac{\partial J}{\partial \mathbf{u}}^T \frac{\partial \mathbf{u}}{\partial \mu_j} \tag{2.6b}$$

The partial derivatives $\frac{\partial \mathbf{u}}{\partial \rho_i}$ and $\frac{\partial \mathbf{u}}{\partial \mu_j}$ are obtained from the equilibrium equation $\mathbf{K}\mathbf{u} = \mathbf{f}$, to obtain:

$$\frac{\partial \mathbf{K}}{\partial \rho_i}\mathbf{u} + \mathbf{K}\frac{\partial \mathbf{u}}{\partial \rho_i} = \cancelto{0}{\frac{\partial \mathbf{f}}{\partial \rho_i}}$$

$$\frac{\partial \mathbf{K}}{\partial \mu_j}\mathbf{u} + \mathbf{K}\frac{\partial \mathbf{u}}{\partial \mu_j} = \cancelto{0}{\frac{\partial \mathbf{f}}{\partial \mu_j}}$$

Here it is assumed that the nodal forces do not depend on the design variables. This is not always true as is the case with self-weight. The case of self-weight and others can be handled provided that the sensitivity is recalculated to account for that[1]. Solving for the derivatives of $\mathbf{u}$ we arrive at:

$$\frac{\partial \mathbf{u}}{\partial \rho_i} = -\mathbf{K}^{-1}\frac{\partial \mathbf{K}}{\partial \rho_i}\mathbf{u}$$

$$\frac{\partial \mathbf{u}}{\partial \mu_j} = -\mathbf{K}^{-1}\frac{\partial \mathbf{K}}{\partial \mu_j}\mathbf{u}$$

which substituted in Equation (2.6) yields:

$$\frac{\mathrm{d}J}{\mathrm{d}\rho_i} = \frac{\partial J}{\partial \rho_i} - \frac{\partial J}{\partial \mathbf{u}}^T \mathbf{K}^{-1}\frac{\partial \mathbf{K}}{\partial \rho_i}\mathbf{u} \tag{2.7a}$$

$$\frac{\mathrm{d}J}{\mathrm{d}\mu_j} = \frac{\partial J}{\partial \mu_j} - \frac{\partial J}{\partial \mathbf{u}}^T \mathbf{K}^{-1}\frac{\partial \mathbf{K}}{\partial \mu_j}\mathbf{u} \tag{2.7b}$$

[1]Topology optimization with self-weight has a tendency to exhibit numerical issues which fall outside the scope of the present work.

For the specific case where the objective function is the structural compliance, i.e. $J = \mathbf{u}^T \mathbf{K}\, \mathbf{u}$, the resulting sensitivities with respect to $\mathbf{u}$, $\rho_i$, and $\mu_j$, are as follows:

$$\frac{\partial J}{\partial \mathbf{u}} = 2\, \mathbf{K}\, \mathbf{u}$$
$$\frac{\partial J}{\partial \rho_i} = \mathbf{u}^T \frac{\partial \mathbf{K}}{\partial \rho_i}\, \mathbf{u}$$
$$\frac{\partial J}{\partial \mu_j} = \mathbf{u}^T \frac{\partial \mathbf{K}}{\partial \mu_j}\, \mathbf{u}$$

which is then plugged into Equation (2.7) to obtain:

$$\frac{\mathrm{d}J}{\mathrm{d}\rho_i} = \mathbf{u}^T \frac{\partial \mathbf{K}}{\partial \rho_i}\, \mathbf{u} - 2\, \mathbf{u}^T\, \mathbf{K}\, \mathbf{K}^{-1} \frac{\partial \mathbf{K}}{\partial \rho_i}\, \mathbf{u}$$
$$\frac{dJ}{d\mu_j} = \mathbf{u}^T \frac{\partial \mathbf{K}}{\partial \mu_j} \mathbf{u} - 2\mathbf{u}^T \mathbf{K} \mathbf{K}^{-1} \frac{\partial \mathbf{K}}{\mu_j} \mathbf{u}$$

Simplifying the former equation, we arrive at the following sensitivities for the specific (yet common) case of compliance as the objective function:

$$\frac{\mathrm{d}J}{\mathrm{d}\rho_i} = -\mathbf{u}^T \frac{\partial \mathbf{K}}{\partial \rho_i}\, \mathbf{u} = -\mathbf{u}_i^T\, \mathbf{K}_0^{(i)} \frac{\partial E^{(i)}}{\partial \rho_i}\, \mathbf{u}_i \tag{2.8a}$$

$$\frac{\mathrm{d}J}{\mathrm{d}\mu_j} = -\mathbf{u}^T \frac{\partial \mathbf{K}}{\partial \mu_j}\, \mathbf{u} = -\sum_{i \in \Omega_j} \mathbf{u}_i^T\, \mathbf{K}_0^{(i)} \frac{\partial E^{(i)}}{\partial \mu_j}\, \mathbf{u}_i \tag{2.8b}$$

where $\mathbf{u}_i$ is the (global) displacement vector associated with the $i$-th element. We note that the sensitivity of $J$ with respect to $\mu_j$ is quite similar to the standard sensitivity with respect to $\rho_i$. The key difference is that the sensitivity for $j$-th $\mu$ variable sums the contributions from all the elements belonging to the subdomain $\Omega_j$. The final missing piece are the derivatives of $E^{(i)}$ with respect to $\rho_i$ and $\mu_j$. It is important to differentiate between the

elements that are part of a subdomain and those which are not. Based on the SIMP power-law, the derivatives result in:

$$\frac{\partial E^{(i)}}{\partial \rho_i} = \begin{cases} (E_0 - E_{min})\, p\, \rho_i^{p-1}\, \mu_j & \forall\, i \in \Omega_j \\ (E_0 - E_{\text{min}})\, p\, \rho_i^{p-1} & \text{otherwise} \end{cases} \tag{2.9a}$$

$$\frac{\partial E^{(i)}}{\partial \mu_j} = (E_0 - E_{min})\, \rho_i^p \tag{2.9b}$$

Finally, substituting into Equation (2.8) the sensitivity of the compliance using a SIMP material interpolation law is:

$$\frac{\mathrm{d}J}{\mathrm{d}\rho_i} = -p\,(E_0 - E_{\text{min}})\, \rho_i^{p-1}\, \mu_j\, \mathbf{u}_i^T\, \mathbf{K}_0^{(i)}\, \mathbf{u}_i \qquad \forall\, i \in \Omega_j \tag{2.10a}$$

$$\frac{\mathrm{d}J}{\mathrm{d}\rho_i} = -p\,(E_0 - E_{\text{min}})\, \rho_i^{p-1}\, \mathbf{u}_i^T\, \mathbf{K}_0^{(i)}\, \mathbf{u}_i \qquad \forall i\ \in \Omega - \bigcup_{j=1}^{N_s} \Omega_j \tag{2.10b}$$

$$\frac{\mathrm{d}J}{\mathrm{d}\mu_j} = -\sum_{i \in \Omega_j} (E_0 - E_{\text{min}})\, \rho_i^p\, \mathbf{u}_i^T\, \mathbf{K}_0^{(i)}\, \mathbf{u}_i \tag{2.10c}$$

In the event that an objective function other than compliance is used, the sensitivities are derived following the same procedure. It should be noted that for most objectives other than compliance, the second term in Equation (2.7) may require an additional linear solve to compute the sensitivities; two actually in our case, one for $\rho_i$ and one for $\mu_i$.

## 2.10. Multiple load cases

The addition of multiple load cases require slightly different treatment involving a modification of the single load case optimization problem in Equation (2.5). Without any loss of generality, the multiple load case derivation here presented considers three different

load scenarios. The ideal optimization problem becomes:

$$
\begin{aligned}
\min_{\mathbf{x},\boldsymbol{\mu}} \quad & \max\left\{ J_1 = \mathbf{u}_1^T\,\mathbf{K}\,\mathbf{u}_1 \quad , \quad J_2 = \mathbf{u}_2^T\,\mathbf{K}\,\mathbf{u}_2 \quad , \quad J_3 = \mathbf{u}_3^T\,\mathbf{K}\,\mathbf{u}_3 \right\} \\
\text{s.t.} \quad & \textstyle\sum_{i=1}^{N} \rho_i\, v_i \leq f_0\, v_0 && \forall\, i \in \Omega \\
& \textstyle\sum_{i=1}^{N_1} \rho_i\, v_i \leq f_1\, v_1 && \forall\, i \in \Omega - \bigcup_{j=1}^{N_s} \Omega_j \\
& \textstyle\sum_{i=1}^{N_2} \rho_i\, v_i \leq f_2\, v_2 && \forall\, i \in \bigcup_{j=1}^{N_s} \Omega_j \\
& \textstyle\sum_{j=1}^{N_s} \mu_j^{1/q} \leq N_0\,(1+\varepsilon) \\
& E^{(i)} = E_{\text{min}} + (E_0 - E_{\text{min}})\,\rho_i^p\,\mu_j && \forall\, i \in \bigcup_{j=1}^{N_s} \Omega_j \\
& E^{(i)} = E_{\text{min}} + (E_0 - E_{\text{min}})\,\rho_i^p && \forall\, i \in \Omega - \bigcup_{j=1}^{N_s} \Omega_j \\
& \boldsymbol{\rho} = \mathbf{H}\,\mathbf{x} \\
& \mathbf{K} = \mathop{\mathsf{A}}_{i=1}^{N} E^{(i)}\,\mathbf{K}_0^{(i)} \\
& 0 \leq x_i \leq 1 && \forall\, i = 1 \ldots N \\
& 0 \leq \mu_j \leq 1 && \forall\, j = 1 \ldots N_s \\
\text{with} \quad & \mathbf{K}\,\mathbf{u}_1 = \mathbf{f}_1 \\
& \mathbf{K}\,\mathbf{u}_2 = \mathbf{f}_2 \\
& \mathbf{K}\,\mathbf{u}_3 = \mathbf{f}_3
\end{aligned}
\tag{2.11}
$$

where $\mathbf{f}_1$, $\mathbf{f}_2$, and $\mathbf{f}_3$, are the nodal load vectors associated with the first, second, and third load cases, respectively. This situation is analogous with the nodal displacements $\mathbf{u}_1$, $\mathbf{u}_2$, and $\mathbf{u}_3$; as well as with the objectives $J_1$, $J_2$, and $J_3$.

The max operator is continuous, yet not continuously differentiable, making the optimization of said objective rather difficult. Therefore, the previous formulation can be relaxed by a similar objective function using the p–norm. In this case, we use the constant $\beta$ to avoid confusion with SIMP power-law penalization constant $p$. The resulting

optimization model is:

$$
\begin{aligned}
\min_{\mathbf{x},\boldsymbol{\mu}} \quad & \left(J_1^\beta + J_2^\beta + J_3^\beta\right)^{1/\beta} \\
\text{s.t.} \quad & \textstyle\sum_{i=1}^{N} \rho_i \, v_i \leq f_0 \, v_0 && \forall \, i \in \Omega \\
& \textstyle\sum_{i=1}^{N_1} \rho_i \, v_i \leq f_1 \, v_1 && \forall \, i \in \Omega - \bigcup_{j=1}^{N_s} \Omega_j \\
& \textstyle\sum_{i=1}^{N_2} \rho_i \, v_i \leq f_2 \, v_2 && \forall \, i \in \bigcup_{j=1}^{N_s} \Omega_j \\
& \textstyle\sum_{j=1}^{N_s} \mu_j^{1/q} \leq N_0 \, (1+\varepsilon) \\
& E^{(i)} = E_{\text{min}} + (E_0 - E_{\text{min}}) \, \rho_i^p \, \mu_j && \forall \, i \in \bigcup_{j=1}^{N_s} \Omega_j \\
& E^{(i)} = E_{\text{min}} + (E_0 - E_{\text{min}}) \, \rho_i^p && \forall \, i \in \Omega - \bigcup_{j=1}^{N_s} \Omega_j \\
& \boldsymbol{\rho} = \mathbf{H} \, \mathbf{x} \\
& \mathbf{K} = \mathop{\mathbf{A}}_{i=1}^{N} E^{(i)} \, \mathbf{K}_0^{(i)} \\
& 0 \leq x_i \leq 1 && \forall \, i = 1 \ldots N \\
& 0 \leq \mu_j \leq 1 && \forall \, j = 1 \ldots N_s \\
\text{with} \quad & \mathbf{K} \, \mathbf{u}_1 = \mathbf{f}_1 \\
& \mathbf{K} \, \mathbf{u}_2 = \mathbf{f}_2 \\
& \mathbf{K} \, \mathbf{u}_3 = \mathbf{f}_3
\end{aligned}
\tag{2.12}
$$

Note that the p–norm optimization problem becomes equivalent to the original problem in Equation (2.11) when $\beta \to \infty$. In this work, the value of $\beta$ was taken as $\beta = 4$.

The manner in which the different objectives are considered can be generalized by means of a combination function $f(\cdot)$ such that $J = f(J_i)$. That is, for the specific case of the formulation presented in Equation (2.11) we have:

$$J = f(J_1 \, , \, J_2 \, , \, J_3 \ldots) = \max_i \, (J_i)$$

whereas for the case presented in Equation (2.12) the combination function is:

$$J = f(J_1\,,\,J_2\,,\,J_3\ldots) = \left(\sum_i J_i^\beta\right)^{1/\beta}$$

Alternative multi-objective formulation, techniques, approaches, and additional combination functions have been historically used (e.g. convex combination, abs–sum, to name a few) but the discussion on these fall out of the scope of the present work. Maintaining the generality on the combination function $f(\cdot)$ chosen, the sensitivity for the multiple load case objective is:

$$\begin{aligned}\frac{\mathrm{d}f}{\mathrm{d}\rho_i} &= \frac{\partial f}{\partial J_1}\left(\frac{\partial J_1}{\partial \rho_i} + \frac{\partial J_1}{\partial \mathbf{u}_1}^T \frac{\partial \mathbf{u}_1}{\partial \rho_i}\right)\ldots \\ &+ \frac{\partial f}{\partial J_2}\left(\frac{\partial J_2}{\partial \rho_i} + \frac{\partial J_2}{\partial \mathbf{u}_2}^T \frac{\partial \mathbf{u}_2}{\partial \rho_i}\right)\ldots \\ &+ \frac{\partial f}{\partial J_3}\left(\frac{\partial J_3}{\partial \rho_i} + \frac{\partial J_3}{\partial \mathbf{u}_3}^T \frac{\partial \mathbf{u}_3}{\partial \rho_i}\right) \end{aligned} \tag{2.13a}$$

$$\begin{aligned}\frac{\mathrm{d}f}{\mathrm{d}\mu_j} &= \frac{\partial f}{\partial J_1}\left(\frac{\partial J_1}{\partial \mu_j} + \frac{\partial J_1}{\partial \mathbf{u}_1}^T \frac{\partial \mathbf{u}_1}{\partial \mu_j}\right)\ldots \\ &+ \frac{\partial f}{\partial J_2}\left(\frac{\partial J_2}{\partial \mu_j} + \frac{\partial J_2}{\partial \mathbf{u}_2}^T \frac{\partial \mathbf{u}_2}{\partial \mu_j}\right)\ldots \\ &+ \frac{\partial f}{\partial J_3}\left(\frac{\partial J_3}{\partial \mu_j} + \frac{\partial J_3}{\partial \mathbf{u}_3}^T \frac{\partial \mathbf{u}_3}{\partial \mu_j}\right) \end{aligned} \tag{2.13b}$$

For the case of the p–norm the derivatives of the objective function with respect to each $J_i$ are:

$$\frac{\partial f}{\partial J_1} = \left(J_1^\beta + J_2^\beta + J_3^\beta\right)^{\frac{1-\beta}{\beta}} J_1^{\beta-1} \tag{2.14a}$$

$$\frac{\partial f}{\partial J_2} = \left(J_1^\beta + J_2^\beta + J_3^\beta\right)^{\frac{1-\beta}{\beta}} J_2^{\beta-1} \tag{2.14b}$$

$$\frac{\partial f}{\partial J_3} = \left(J_1^\beta + J_2^\beta + J_3^\beta\right)^{\frac{1-\beta}{\beta}} J_3^{\beta-1} \tag{2.14c}$$

The partial derivatives of $\mathbf{u}$ with respect to $\rho_i$ and $\mu_j$ are the same as with the single load case scenario (again assuming the loads are not design-dependent). Substituting these in

Equation (2.13) for each load case and expanding we arrive at:

$$\begin{aligned}\frac{\mathrm{d}f}{\mathrm{d}\rho_i} &= \frac{\partial f}{\partial J_1}\left(\mathbf{u}_1^T\frac{\partial \mathbf{K}}{\partial \rho_i}\mathbf{u}_1 - 2\mathbf{u}_1^T\mathbf{K}\mathbf{K}^{-1}\frac{\partial \mathbf{K}}{\partial \rho_i}\mathbf{u}_1\right)\dots \\ &+ \frac{\partial f}{\partial J_2}\left(\mathbf{u}_2^T\frac{\partial \mathbf{K}}{\partial \rho_i}\mathbf{u}_2 - 2\mathbf{u}_2^T\mathbf{K}\mathbf{K}^{-1}\frac{\partial \mathbf{K}}{\partial \rho_i}\mathbf{u}_2\right)\dots \\ &+ \frac{\partial f}{\partial J_3}\left(\mathbf{u}_3^T\frac{\partial \mathbf{K}}{\partial \rho_i}\mathbf{u}_3 - 2\mathbf{u}_3^T\mathbf{K}\mathbf{K}^{-1}\frac{\partial \mathbf{K}}{\partial \rho_i}\mathbf{u}_3\right) \qquad (2.15a)\end{aligned}$$

$$\begin{aligned}\frac{\mathrm{d}f}{\mathrm{d}\mu_j} &= \frac{\partial f}{\partial J_1}\left(\mathbf{u}_1^T\frac{\partial \mathbf{K}}{\partial \mu_j}\mathbf{u}_1 - 2\mathbf{u}_1^T\mathbf{K}\mathbf{K}^{-1}\frac{\partial \mathbf{K}}{\partial \mu_j}\mathbf{u}_1\right)\dots \\ &+ \frac{\partial f}{\partial J_2}\left(\mathbf{u}_2^T\frac{\partial \mathbf{K}}{\partial \mu_j}\mathbf{u}_2 - 2\mathbf{u}_2^T\mathbf{K}\mathbf{K}^{-1}\frac{\partial \mathbf{K}}{\partial \mu_j}\mathbf{u}_2\right)\dots \\ &+ \frac{\partial f}{\partial J_3}\left(\mathbf{u}_3^T\frac{\partial \mathbf{K}}{\partial \mu_j}\mathbf{u}_3 - 2\mathbf{u}_3^T\mathbf{K}\mathbf{K}^{-1}\frac{\partial \mathbf{K}}{\partial \mu_j}\mathbf{u}_3\right) \qquad (2.15b)\end{aligned}$$

These sensitivities can be further simplified and expanded using each finite element's contribution:

$$\begin{aligned}\frac{\mathrm{d}f}{\mathrm{d}\rho_i} &= \frac{\partial f}{\partial J_1}\left(-\mathbf{u}_{1i}^T\mathbf{K}_0^{(i)}\frac{\partial E_i}{\partial \rho_i}\mathbf{u}_{1i}\right)\dots \\ &+ \frac{\partial f}{\partial J_2}\left(-\mathbf{u}_{2i}^T\mathbf{K}_0^{(i)}\frac{\partial E_i}{\partial \rho_i}\mathbf{u}_{2i}\right)\dots \\ &+ \frac{\partial f}{\partial J_3}\left(-\mathbf{u}_{3i}^T\mathbf{K}_0^{(i)}\frac{\partial E_i}{\partial \rho_i}\mathbf{u}_{3i}\right) \qquad (2.16a)\end{aligned}$$

$$\begin{aligned}\frac{\mathrm{d}f}{\mathrm{d}\mu_j} &= \frac{\partial f}{\partial J_1}\left(-\sum_{i\in\Omega_j}\mathbf{u}_{1i}^T\mathbf{K}_0^{(i)}\frac{\partial E_i}{\partial \mu_j}\mathbf{u}_{1i}\right)\dots \\ &+ \frac{\partial f}{\partial J_2}\left(-\sum_{i\in\Omega_j}\mathbf{u}_{2i}^T\mathbf{K}_0^{(i)}\frac{\partial E_i}{\partial \mu_j}\mathbf{u}_{2i}\right)\dots \\ &+ \frac{\partial f}{\partial J_3}\left(-\sum_{i\in\Omega_j}\mathbf{u}_{3i}^T\mathbf{K}_0^{(i)}\frac{\partial E_i}{\partial \mu_j}\mathbf{u}_{3i}\right) \qquad (2.16b)\end{aligned}$$

It is then clear, that analogous to the single load case, the sensitivity with respect to $\rho_i$ associated with the $i$-th element, is calculated using element local information of that specific element. On the other hand, the sensitivity with respect to $\mu_j$ adds the contributions

of all elements that belong to the $j$-th subdomain, which is also analogous in the single load case scenario.

### 2.10.1. $\alpha_i$ constants

Optimized structures subjected to multiple load cases do not always perform equally under each one of them. A trivial proof of this occurs when a second load case is equal to a scaled-down version of the first one. Another example of this happens in high-rise building design; the design of these structures is more sensitive to load combinations that include wind in them. Similarly, buildings with an asymmetric footprint[2] buildings are prone to high torsional drifts due to seismic loads.

The multiple load case formulation previously presented takes into account the performance of the structure towards each load case by multiplying the sensitivities of each load case by a constant $\alpha_i$, which is the derivative of the combined p–norm objective with respect to $J_i$, as defined in Equation (2.14). The relative value of these constants is associated with the sensitivity of the design for each load case. Therefore, the final values of the constants $\alpha_i$ illustrate the relative importance of each load case in the resulting topology.

## 2.11. Alternative objective functions

The structural compliance is a convenient objective function which is very commonly used in structural topology optimization. Its popularity is explained by two facts: its physical outcome is to minimize the displacements associated with the load points (stiffest structure), and the sensitivity calculation is trivial since it is a *self-adjoint function*. The derivations carried out in the previous sections are often developed for the specific case of compliance, which makes the explanations simpler. However, the work here presented

[2]An asymmetric building footprint will cause the center of mass and the center of stiffness to be relatively far from each other. This results in an accidental torsion on the building when subjected to a transverse seismic acceleration.

can all be extended to consider objectives other than compliance, and one such relevant case is derived below.

Building design, for example, often involves objectives (and restrictions) associated with drift or specific displacements (Taranath, 2016). To minimize the top-floor drift, is equivalent to minimizing the square of said value, which is the dot product of a vector containing the drift in the $\hat{\mathbf{x}}$ and $\hat{\mathbf{y}}$ directions. In this case, the objective function is $J = \mathbf{u}^T \mathbf{D}^T \mathbf{D}\, \mathbf{u}$. Here $\mathbf{D}$ is a transformation matrix of $2 \times N_{\text{dof}}$ which calculates the average roof displacement in the $\hat{\mathbf{x}}$ and $\hat{\mathbf{y}}$ directions (hence the two rows) from the displacement vector $\mathbf{u}$ of length equal to $N_{\text{dof}}$ (number of degrees of freedom).

The sensitivities for this new objective use the adjoint method (Tortorelli & Michaleris, 1994; Christensen & Klarbring, 2009). First, we define an augmented objective function:

$$J^\star(\mathbf{x}) = \mathbf{u}^T \mathbf{D}^T \mathbf{D}\, \mathbf{u} + \boldsymbol{\lambda}_J^T \left(\mathbf{K}\, \mathbf{u} - \mathbf{f}\right) \tag{2.17}$$

Here $\boldsymbol{\lambda}_J$ is the adjoint vector and is an arbitrary vector. Note that nothing is really added to the objective since structural equilibrium is enforced in the nested problem and is therefore equal to $\mathbf{0}$. The partial derivatives $\frac{\mathrm{d}J^\star}{\mathrm{d}\rho_i}$ and $\frac{\mathrm{d}J^\star}{\mathrm{d}\mu_j}$ are:

$$\begin{aligned}\frac{\mathrm{d}J^\star}{\mathrm{d}\rho_i} &= \frac{\partial \mathbf{u}^T}{\partial \rho_i} \mathbf{D}^T \mathbf{D}\, \mathbf{u} + \mathbf{u}^T \mathbf{D}^T \mathbf{D} \frac{\partial \mathbf{u}}{\partial \rho_i} \dots \\ &\quad + \boldsymbol{\lambda}_J^T \left( \frac{\partial \mathbf{K}}{\partial \rho_i} \mathbf{u} + \mathbf{K} \frac{\partial \mathbf{u}}{\partial \rho_i} - \frac{\partial \mathbf{f}}{\partial \rho_i} \right) \end{aligned} \tag{2.18a}$$

$$\begin{aligned}\frac{\mathrm{d}J^\star}{\mathrm{d}\mu_j} &= \frac{\partial \mathbf{u}^T}{\partial \mu_j} \mathbf{D}^T \mathbf{D}\, \mathbf{u} + \mathbf{u}^T \mathbf{D}^T \mathbf{D} \frac{\partial \mathbf{u}}{\partial \mu_j} \dots \\ &\quad + \boldsymbol{\lambda}_J^T \left( \frac{\partial \mathbf{K}}{\partial \mu_j} \mathbf{u} + \mathbf{K} \frac{\partial \mathbf{u}}{\partial \mu_j} - \frac{\partial \mathbf{f}}{\partial \mu_j} \right) \end{aligned} \tag{2.18b}$$

Simplifying and assuming that the nodal forces do not depend on the design variables we obtain:

$$\frac{\mathrm{d}J^\star}{\mathrm{d}\rho_i} = 2\mathbf{u}^T\,\mathbf{D}^T\,\mathbf{D}\,\frac{\partial\mathbf{u}}{\partial\rho_i} + \boldsymbol{\lambda}_J^T\left(\frac{\partial\mathbf{K}}{\partial\rho_i}\,\mathbf{u} + \mathbf{K}\,\frac{\partial\mathbf{u}}{\partial\rho_i} - \frac{\partial\mathbf{f}}{\partial\rho_i}\right) \tag{2.19a}$$

$$\frac{\mathrm{d}J^\star}{\mathrm{d}\mu_j} = 2\mathbf{u}^T\,\mathbf{D}^T\,\mathbf{D}\,\frac{\partial\mathbf{u}}{\partial\mu_j} + \boldsymbol{\lambda}_J^T\left(\frac{\partial\mathbf{K}}{\partial\mu_j}\,\mathbf{u} + \mathbf{K}\,\frac{\partial\mathbf{u}}{\partial\mu_j} - \frac{\partial\mathbf{f}}{\partial\mu_j}\right) \tag{2.19b}$$

Since $\boldsymbol{\lambda}_J$ is arbitrary, we one that cancels $\frac{\partial\mathbf{u}^T}{\partial\rho_i}$ and $\frac{\partial\mathbf{u}^T}{\partial\mu_j}$. This results in the following adjoint problem:

$$2\mathbf{u}^T\,\mathbf{D}^T\,\mathbf{D} + \boldsymbol{\lambda}_J^T\,\mathbf{K} = 0 \tag{2.20}$$

, and solving for $\boldsymbol{\lambda}_J$ we obtain:

$$\boldsymbol{\lambda}_J = \mathbf{K}^{-1}\,\left(-2\,\mathbf{D}^T\,\mathbf{D}\,\mathbf{u}\right) \tag{2.21}$$

Substituting the value of $\boldsymbol{\lambda}_J$ into Equation (2.19):

$$\frac{\mathrm{d}J^\star}{\mathrm{d}\rho_i} = \mathbf{K}^{-1}\,\left(-2\mathbf{D}^T\,\mathbf{D}\,\mathbf{u}\right)\,\frac{\partial\mathbf{K}}{\partial\rho_i}\,\mathbf{u} \tag{2.22a}$$

$$\frac{\mathrm{d}J^\star}{\mathrm{d}\mu_j} = \mathbf{K}^{-1}\,\left(-2\mathbf{D}^T\,\mathbf{D}\,\mathbf{u}\right)\,\frac{\partial\mathbf{K}}{\partial\mu_j}\,\mathbf{u} \tag{2.22b}$$

The remaining derivation follows the same procedure shown for compliance as the objective function; the sensitivity using a SIMP material interpolation law becomes:

$$\frac{\mathrm{d}J^\star}{\mathrm{d}\rho_i} = \boldsymbol{\lambda}_J\,\left[p\,(E_0 - E_{\text{min}})\,\rho_i^{p-1}\,\mu_j\,\mathbf{u}_i^T\,\mathbf{K}_0^{(i)}\,\mathbf{u}_i\right] \qquad \forall\ i \in \Omega_j \tag{2.23a}$$

$$\frac{\mathrm{d}J^\star}{\mathrm{d}\rho_i} = \boldsymbol{\lambda}_J\,\left[p\,(E_0 - E_{\text{min}})\,\rho_i^{p-1}\,\mathbf{u}_i^T\,\mathbf{K}_0^{(i)}\,\mathbf{u}_i\right] \qquad \forall i\ \in \Omega - \bigcup_{j=1}^{N_s}\Omega_j \tag{2.23b}$$

$$\frac{\mathrm{d}J^\star}{\mathrm{d}\mu_j} = \sum_{i\in\Omega_j}\boldsymbol{\lambda}_J\,\left[(E_0 - E_{\text{min}})\,\rho_i^{p}\,\mathbf{u}_i^T\,\mathbf{K}_0^{(i)}\,\mathbf{u}_i\right] \tag{2.23c}$$

where $\boldsymbol{\lambda}_J$ is the value obtained from solving the adjoint problem (Equation (2.21)). It should be noted that the adjoint method requires a single additional solution of the state equation (Equation (2.21)) to calculate the objective function sensitivities for all design variables (regardless of their number). The exception being compliance as an objective,

where the adjoint problem is equivalent to the equilibrium equation (i.e. compliance is self-adjoint). From this point onward, considering multiple load cases is analogous to the previously shown case (compliance).

The formulation constraints are dealt in a similar fashion. For any given constraint $g(\mathbf{x}) \leq c$, with $c$ being some scalar constant, the augmented adjoint form becomes:

$$g^{\star}(\mathbf{x}) = g(\mathbf{x}) + \boldsymbol{\lambda}_g^T \left(\mathbf{K}\,\mathbf{u} - \mathbf{f}\right) \leq c \tag{2.24}$$

The partial derivative $\frac{\mathrm{d}g^{\star}}{\mathrm{d}\rho_i}$ becomes:

$$\frac{\mathrm{d}g^{\star}}{\mathrm{d}\rho_i} = \frac{\partial g}{\partial \rho_i} + \frac{\partial g}{\partial \mathbf{u}}\frac{\partial \mathbf{u}}{\partial \rho_i} + \boldsymbol{\lambda}_g^T \left(\frac{\partial \mathbf{K}}{\partial \rho_i}\mathbf{u} + \mathbf{K}\frac{\partial \mathbf{u}}{\partial \rho_i} - \frac{\partial \mathbf{f}}{\partial \rho_i}\right) \tag{2.25}$$

Thus, assuming the loads do not depend on the design variables, the adjoint problem associated with this constraint becomes:

$$\boldsymbol{\lambda}_g = \mathbf{K}^{-1}\left(-\frac{\partial g}{\partial \mathbf{u}}\right) \tag{2.26}$$

After the adjoint vector $\boldsymbol{\lambda}_g$ is solved for, it can be replaced in Equation (2.25) where it is clear that the dependency of the sensitivity with respect to the displacements $\mathbf{u}$ is no longer an issue. Finally, the sensitivity sought for is:

$$\frac{\mathrm{d}g}{\mathrm{d}x_i} = \frac{\mathrm{d}g}{\mathrm{d}\boldsymbol{\rho}}\frac{\mathrm{d}\boldsymbol{\rho}}{\mathrm{d}x_i}$$

Analogous to the previous case of the objective function; the adjoint method requires a single additional solution of the state equation (Equation (2.21)) to calculate the constraint sensitivities for all design variables (regardless of their number). The volume constraint is a trivial situation since $\frac{\partial g}{\partial \mathbf{u}} = \mathbf{0}$, and therefore no adjoint solution is necessary. This is not the case, however, for a displacement limit; e.g. a *drift* limit on a building. The sensitivity with respect to the subdomain design variables $\boldsymbol{\mu}$ follows the same procedure described above.

# 3. EXAMPLES

The following examples aim to highlight the capabilities and limitations of the proposed method. The examples include 2D and 3D problems: the 2D examples use Q4 (4-noded quadrilateral) finite elements, whereas the 3D examples make use of a plane quadrilateral shell element. The plane shell element is based on the superposition of a Q4D4 membrane element with a P4 plate element (Oñate, 2013).

## 3.1. Leaning towers

This example considers two cantilever towers connected by a series of consecutive subdomains. Symmetry is enforced within each tower and among both towers along the vertical axis. In addition, the subdomains have enforced symmetry with respect to their central vertical axis. The goal of the subdomains is to offload the lateral force to the second (unloaded) tower such that the overall behavior is optimal. Because the problem is linear-elastic and there is only one load case, the magnitude of the distributed load applied is irrelevant (only the shape of the diagram matters). The applied distributed load is uniform with a value $q = 1$. On the other hand, the domain has a thickness $t = 1$ and elastic modulus $E_0 = 10^5$ GPa. The relative dimensionality of the load, thickness, and elastic modulus is only relevant within the context of the parameters used by the MMA algorithm (optimizer).

This problem has a limit on the volume fraction $f_0$ for the complete domain, and a limit on the volume fraction $f_2$ of the subdomains. The volume fraction $f_1$ for the elements outside of the subdomains is unrestricted (i.e. $f_1 = 1$). The lateral edges of the towers consider a vertical passive-solid column of two elements in width to support and distribute the applied load. The loads and supports are presented in Figure 3.1, whereas the design domain with all the possible subdomains is presented in Figure 3.2.

Results are obtained for two distinct sets of optimization parameters. The element size, density filter, and penalizations $p$ and $q$ are the same in both cases. The structure in

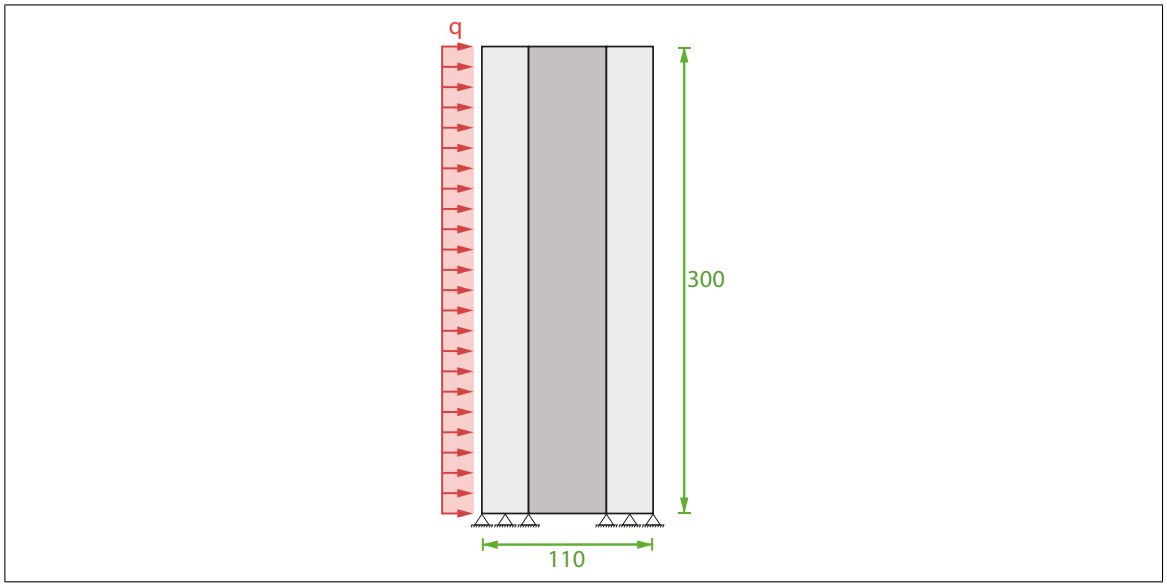


Figure 3.1. Leaning towers loads and supports.

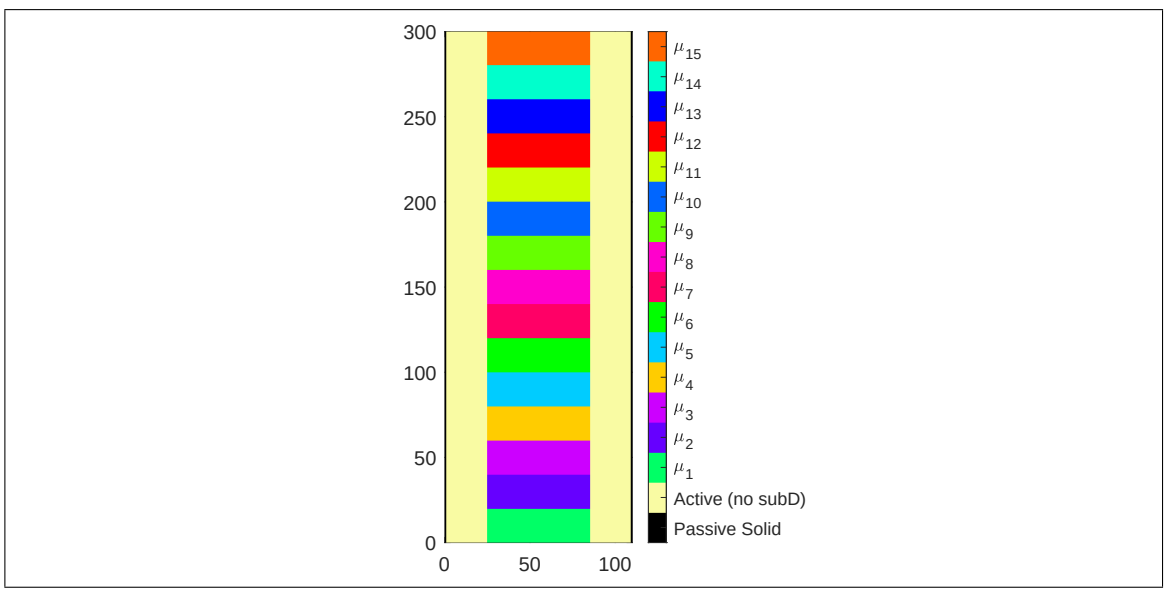


Figure 3.2. Leaning towers design domain (including subdomains).

Figure 3.3(a) was run with a desired total number of subdomains $N_0$ equal to three and with the following volume fractions: $f_0 = 0.3$, $f_1 = 1$, and $f_2 = 0.03$. The finite elements have a size equal to $0.6250 \times 0.2500$. The density filter has an initial radius $r_{min} = 1.75$, and is reduced through a continuation scheme to a final value of $r_{min} = 0$ (no filter) in the

last set of iterations. The penalization $p$ of the element density $\boldsymbol{\rho}$ and the penalization $q$ of the subdomains $\boldsymbol{\mu}$ started at $1.25$ and $1.75$, respectively, and a continuation was applied until they reached $4.5$ and $4.0$, respectively. On the other hand, the results in Figure 3.3(b) were obtained using a desired total number of subdomains $N_0$ equal to four and with the following volume fractions: $f_0 = 0.3$, $f_1 = 1$, and $f_2 = 0.1$.

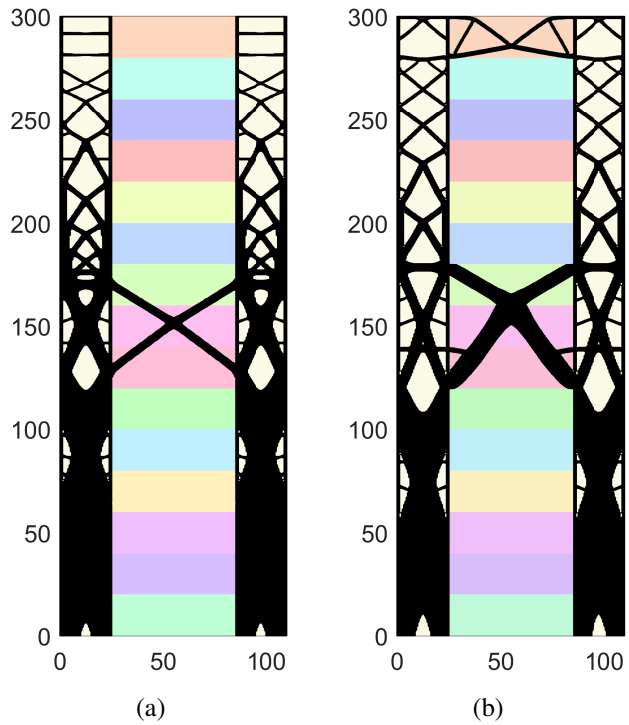


Figure 3.3. Optimized structure for the leaning towers: **(a)** case with three available subdomains (i.e. $N_0 = 3$); and **(b)** case with four available subdomains (i.e. $N_0 = 4$).

It can be seen that for both sets of parameters, the algorithm correctly chooses the desired number of subdomains, with three in Figure 3.3(a) and four in Figure 3.3(b). The solution in Figure 3.3(a) utilizes the subdomains $\mu_7$, $\mu_8$, and $\mu_9$. The towers are connected by a large X-brace spanning all three subdomains. On the other hand, the solution presented in Figure 3.3(b) shows that the optimal subdomains are $\mu_7$, $\mu_8$, $\mu_9$, and $\mu_{15}$. In this case, the towers are also connected by a large brace spanning three subdomains, but in

addition to this, there is a head-truss at the top level of the towers. The intersection of the cross is not central as in the previous solution, but it is rather displaced towards the top, which is also known to be quite optimal (Zegard et al., 2014).

The solutions obtained for this example exhibit a large concentration of material towards the base. This behavior is expected and documented in literature: the lack of a third out-of-plane dimension causes the material to concentrate near the base resulting in a near solid topology (Stromberg et al., 2012). Moreover, in engineering practice, it is not advisable to link two towers as the solutions suggest. However, this rather simplistic problem showcases the capability of the proposed method to simultaneously select the subdomains and optimize the structure. The results obtained are not always intuitive and depend on the number of subdomains available for the algorithm to use.

### 3.2. 2D bridge

This example considers a 2D bridge where the subdomains correspond to possible support piers. For this problem, the bridge's deck is pinned at both ends and is modeled as a passive-solid element over which a uniform distributed downwards load is applied. The base of the subdomains are also pinned to the ground. The goal is to find the optimal pier location (or locations), as well as their topological design. Because the problem is linear-elastic and there is only one load case, the magnitude of the distributed load $q$ applied is irrelevant. Therefore, the applied load is $q = 1$ and also the elastic modulus $E_0$ is $E_0 = 1$ and the thickness $t$ of the Q4 elements is $t = 1$.

The loads and supports are presented in Figure 3.4, while the design domain with all the possible subdomains is presented in Figure 3.5.

Results are obtained for two distinct sets of optimization parameters. The element size, density filter, and penalizations $p$ and $q$ are the same in both cases. The structure in Figure 3.6(a) was run with a desired total number of subdomains $N_0$ equal to two and with the following volume fractions: $f_0 = 0.2$, $f_1 = 0.35$, and $f_2 = 0.15$. The finite elements

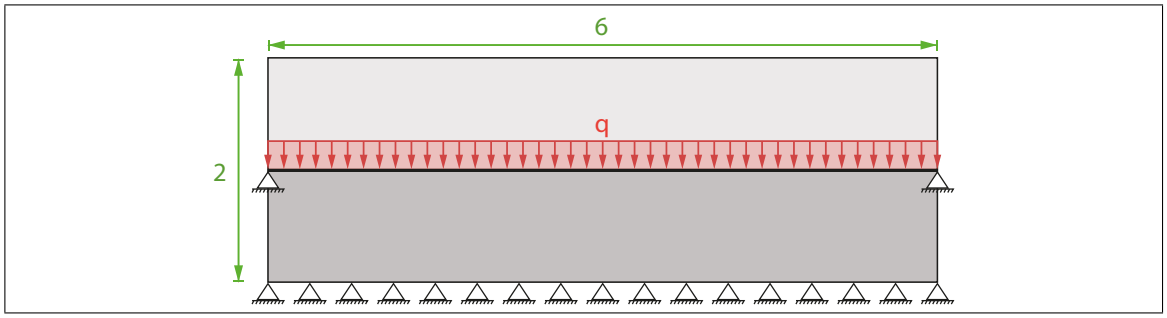


Figure 3.4. 2D bridge loads and supports.

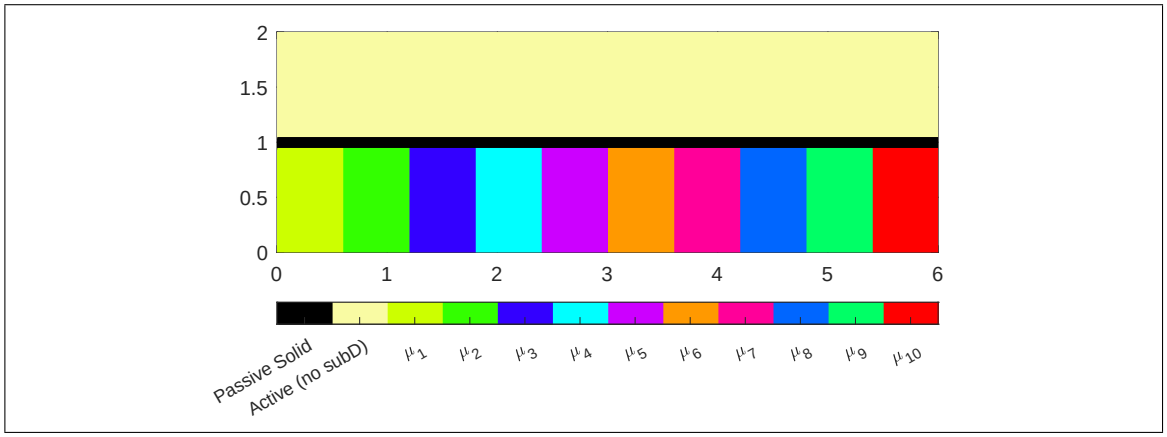


Figure 3.5. 2D bridge design domain (including subdomains).

have a size equal to $0.0150 \times 0.0167$. The density filter has an initial radius $r_{min} = 0.07$, and is reduced through a continuation scheme to a final value of $r_{min} = 0.03$ in the last set of iterations. The penalization $p$ of the element density $\boldsymbol{\rho}$ and the penalization $q$ of the subdomains $\boldsymbol{\mu}$ started at $1.25$ and $1.75$, respectively, and a continuation was applied until they reached $4.5$ and $4.0$, respectively. On the other hand, the results in Figure 3.6(b) were obtained using a desired total number of subdomains $N_0$ equal to four and with the following volume fractions: $f_0 = 0.2$, $f_1 = 0.25$, and $f_2 = 0.15$.

It can be seen that for both sets of parameters, the algorithm correctly chooses the desired number of subdomains, with two in Figure 3.6(a) and four in Figure 3.6(b). Both solutions are similar to one another. The solution with two subdomains in Figure 3.6(a) suggests that the optimal location of the piers is at the middle. The resulting piers are

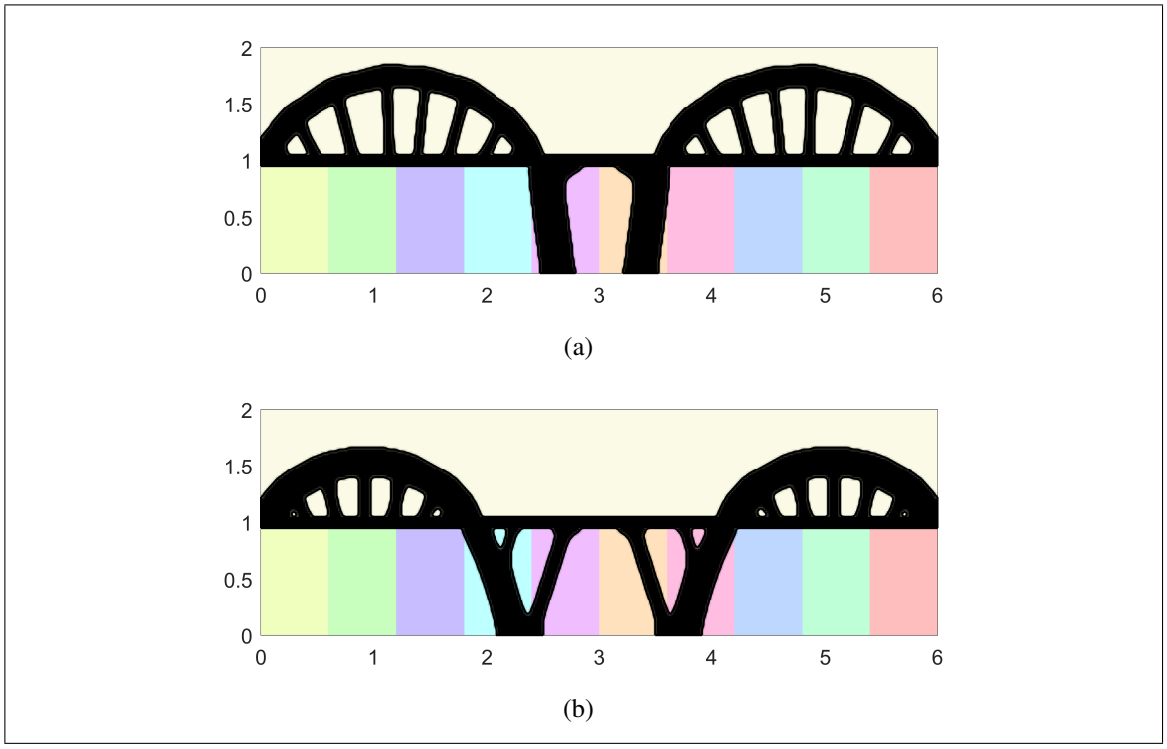


Figure 3.6. Optimized structure for the 2D bridge: **(a)** case with two available subdomains (i.e. $N_0 = 2$); and **(b)** case with four available subdomains (i.e. $N_0 = 4$).

inclined to better receive the loads from the two arches above. On the other hand, the solution with four subdomains presented in Figure 3.6(b) selects the optimal subdomains $\mu_4$, $\mu_5$, $\mu_6$, and $\mu_7$. It can be seen that the algorithm builds on the previous solution in order to solve the problem using four subdomains by reducing the span of the arches. The optimal pier locations and the number of spans depend on the problem's geometry (mainly height and span), and the loading conditions. In that regard, it can be said that the optimal solution structure will also depend on the number of subdomains (piers) available for the algorithm to use.

### 3.3. Castellated beam

In this example, we model a 3D version of a castellated steel I-beam, which is inspired in Example 1 of AISC Steel Design Guide 31 (Fares et al., 2016). Here the subdomains

are associated to the potential web openings in the beam. In this case, the interest is placed on the pair of openings (due to symmetry) that when filled will benefit the beam behavior the most.

This problem includes passive-solid elements that correspond to the web (minus the openings) and flanges. With respect to the supports: the web at both endpoints are supported on both $\hat{\mathbf{y}}$ and $\hat{\mathbf{z}}$ directions; the web center node at a single end is also supported on the $\hat{\mathbf{x}}$ direction. These support conditions approximate a shear-only connection of the beam. However, in order to reduce computational costs, the symmetry of the problem is considered. This reduces the problem to only one-half of the original beam. The nodes originally located at the middle of the beam are supported on the $\hat{\mathbf{x}}$ direction and rotations in $\hat{\mathbf{y}}$ and $\hat{\mathbf{z}}$ are also prevented (symmetry condition).

The loads follow those defined within Example 1 of AISC Steel Design Guide 31. The live load $L$ is $100$ lb/ft while the dead load $D$ is $139$ lb/ft, which includes beam self-weight. These loads are applied on the center nodes of the top flange of the beam. Therefore, the load combination to be used is $1.2D + 1.6L$.

The loads and supports are presented within a repeatable unit cell of the complete domain in Figure 3.7 using a relatively coarse mesh. Figure 3.8 presents the mesh used in a single cell (repeatable unit) of the complete design domain. The fully assembled design domain is shown in Figure 3.9 and repeats the unit cell 36 times, in addition to a solid margin near the endpoints. It is important to mention that due to symmetry, only half of the problem is relevant: there are only 18 combinations of selectable subdomains.

This problem was run with one set of parameters. The structure in Figure 3.10 was run with a desired total number of subdomains $N_0$ equal to one, which considering symmetry is eventually two subdomains. The following volume fractions were used: $f_0 = 0.7$, $f_1 = 1$, and $f_2 = 0.1$. The density filter has an initial radius $r_{min} = 0.5$, and is reduced through a continuation scheme to a final value of $r_{min} = 0$ (no filter) in the last set of iterations. The penalization $p$ of the element density $\boldsymbol{\rho}$ and the penalization $q$ of the subdomains $\boldsymbol{\mu}$

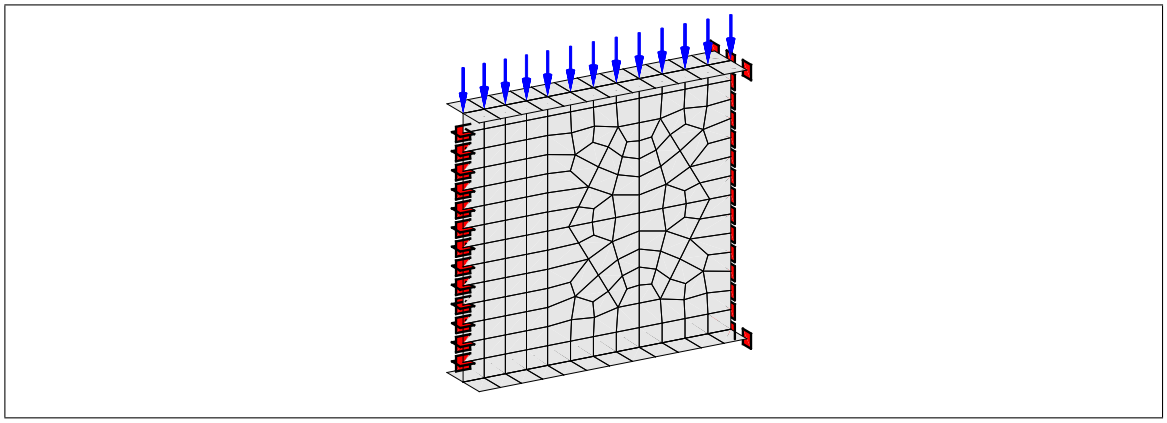

Figure 3.7. Castellated beam unit cell with loads and supports using a coarse mesh.

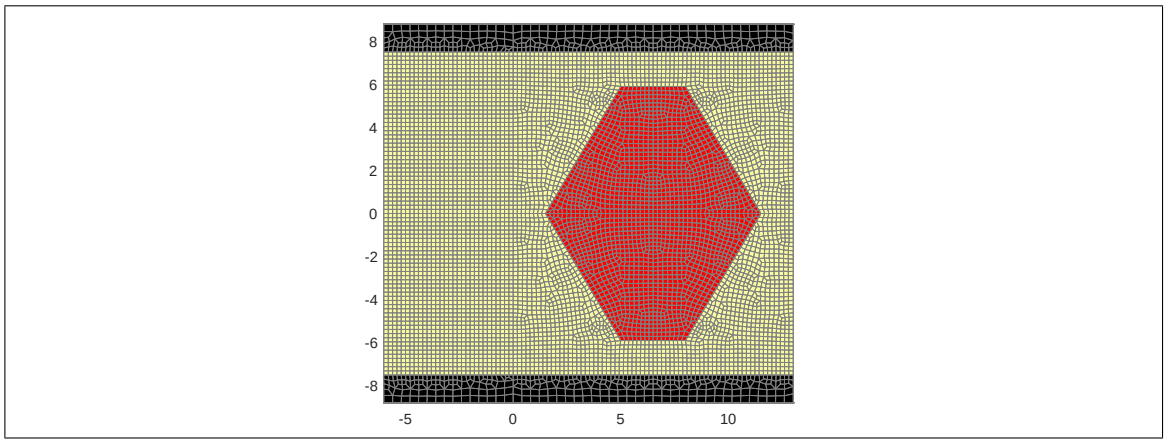


Figure 3.8. Castellated beam cell mesh (repeatable unit).

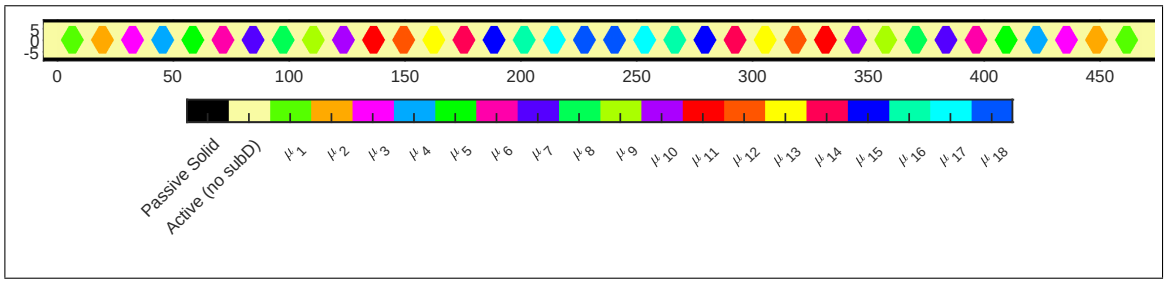


Figure 3.9. Castellated beam design domain with the unit cell repeated 36 times.

started at $1.75$ and a continuation was applied until they both reached $4.5$ at the same iteration.

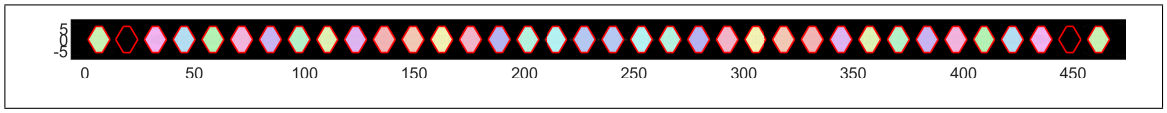


Figure 3.10. Optimized structure for castellated beam with $N_0 = 2$.

It can be seen that the algorithm correctly chooses the desired number of subdomains, with two (after symmetry is applied) in Figure 3.10. The solution shows that the optimal subdomain is $\mu_2$, which is symmetrically replicated on the right side. Also, all the openings are completely empty and do not have material in them, except for the chosen subdomain. It is important to mention that the chosen subdomains are near the ends of the beam. This is most likely because the shear force in a simply supported beam with a distributed load along its span is maximum at the ends. Therefore, by including more material in the web, the shear force can be better addressed.

### 3.4. 3D bridge

This example considers a three-dimensional bridge supported by a finite number of piers along its length. The bridge is composed of a deck, four longitudinal beams, and 12 piers. The subdomains correspond to the piers of the structure. The piers have five shear keys each, which are passive solid elements that sit between the four deck beams. The deck and beams are also passive-solid elements which also do not belong to any subdomain. This structure has three load cases applied:

(i) Distributed pressure load on the right half the deck loaded.
(ii) Distributed pressure load on the left half of the deck loaded.
(iii) Distributed pressure load over the entire deck.

All loads are pressures of magnitude $q = 1$. The structure is supported at the bridge endpoints by constraining displacement on the $\hat{\mathbf{z}}$ direction. The same restriction is applied to both ends of the four deck beams. The center line of the endpoint nodes at deck level have their displacement in the $\hat{\mathbf{x}}$ direction constrained. The piers have all their nodes at the base with a fixed boundary condition. These load cases and support conditions are

illustrated in Figures 3.11(a), 3.11(b), and 3.11(c). While the design domain with all the possible subdomains is presented in Figures 3.12 and 3.13.

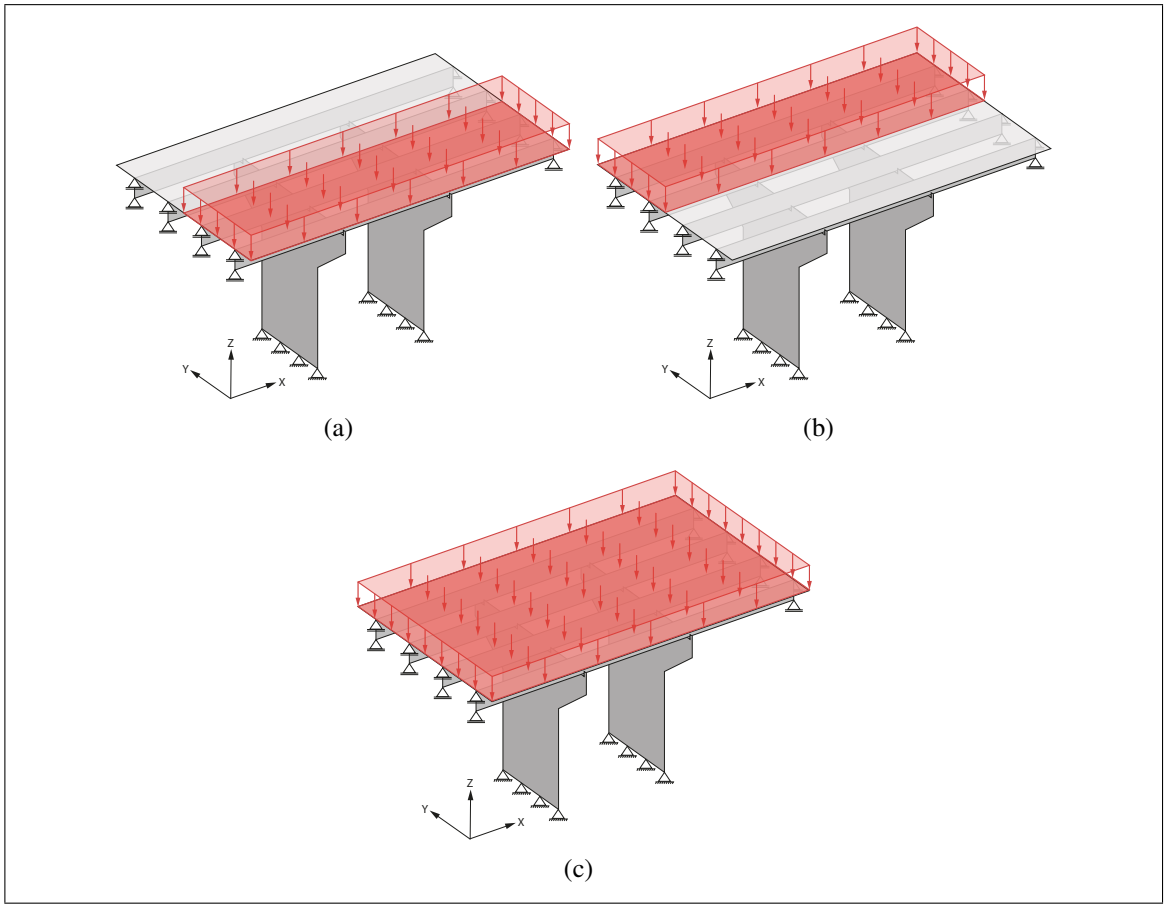


Figure 3.11. 3D bridge load cases: **(a)** right lane loaded; **(b)** left lane loaded; and **(a)** both lanes loaded.

This problem was run with one set of parameters. It was run with a desired total number of subdomains $N_0$ equal to four and with the following volume fractions: $f_0 = f_1 = 1$ and $f_2 = 0.2$. The density filter has an initial radius $r_{min} = 0.5$, and is reduced through a continuation scheme to a final value of $r_{min} = 0.01$ in the last set of iterations. The penalization $p$ of the element density $\boldsymbol{\rho}$ and the penalization $q$ of the subdomains $\boldsymbol{\mu}$ started at $1.25$ and $1.75$, respectively, and a continuation was applied until they both reached $4.0$.

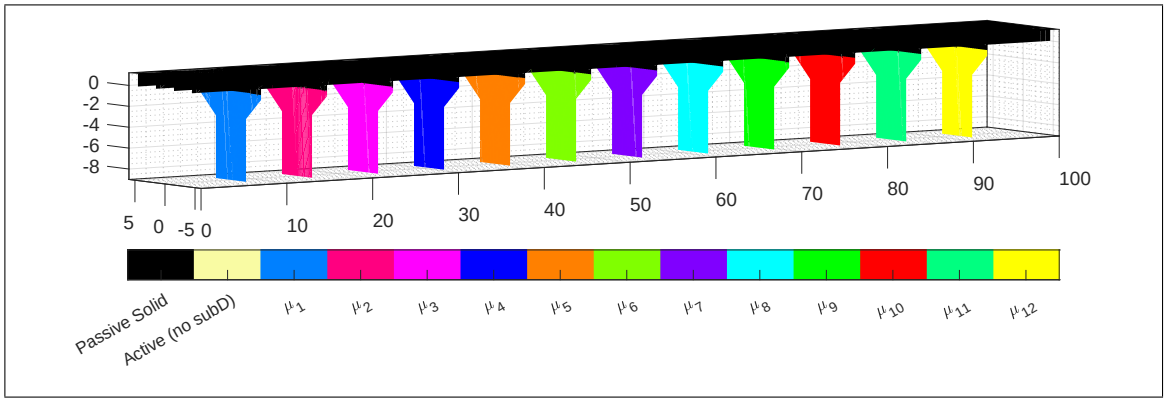


Figure 3.12. 3D bridge domain isometric view.

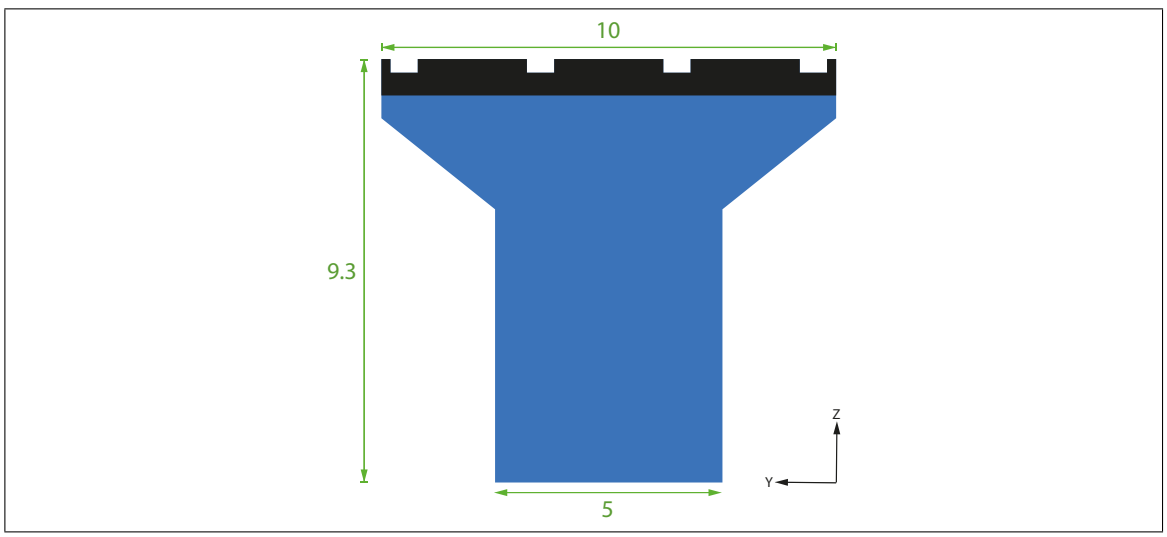


Figure 3.13. 3D bridge domain front view.

As mentioned before, this problem considers three load cases. Each load case has an associated coefficient $\alpha_i$ which correspond to the objective weights in Equation (2.14) and further described in Section 2.10.1. The final values for the coefficients $\alpha_i$ are:

$$\begin{bmatrix}\alpha_1 & \alpha_2 & \alpha_3\end{bmatrix} = \begin{bmatrix}0.5756 & 0.5756 & 0.0934\end{bmatrix} \tag{3.1}$$

The final values of the constants $\alpha_i$ suggest that the algorithm decided to prioritize load cases presented in Figure 3.11(a) and Figure 3.11(b), rather than the load case with both lanes loaded. This result is expected because loading only one of the two lanes generates

a larger overturning moment on the deck than loading both lanes at the same time. The optimized structure for the three load cases is presented in Figure 3.14.

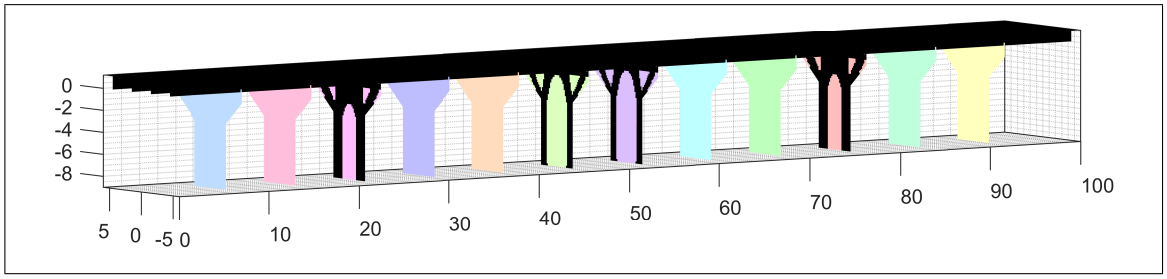


Figure 3.14. P-norm structure for 3D bridge using $N_0 = 4$.

It can be seen that the algorithm correctly chooses the desired number of subdomains, with 4 in Figure 3.14. The solution shows that the optimal subdomains are $\mu_3$, $\mu_6$, $\mu_7$ and $\mu_{10}$. The two central piers possess a different shape than the two external piers. The two external piers collect the bridge deck using three arms, two external and one central, whereas the two central piers require 4 distinct arms. Also, the columns and arms in the external piers use more material than the ones in the 2 central piers.

### 3.5. High-rise building with outriggers

In this example, we model a three-dimensional 84-story high-rise tower with a prismatic floor-plan of dimension $27 \times 18$ m, with a total building height of $269.2$ m. The high-rise tower is designed with outriggers to improve performance and they are the key component in the design optimization. The structural model is composed of a core, slabs, 12 perimeter columns, and the outrigger system. The outrigger system has 8 panels per floor that connect the vertices of the square core with corresponding 8 perimeter columns (the corner columns are not connected to the outrigger system directly). A single design subdomain is considered as three consecutive floors; the 84-story tower has 28 subdomains. The core and slabs are passive-solids elements making the outrigger panels the only design domains. The loads applied are dead, live, and wind loads. The live loads correspond to office live loads and roof live loads, which are applied directly on the slabs.

The dead loads correspond to the self-weight of the concrete slabs and core [1]. The outriggers do not have loads applied because they correspond to the design domain and their self-weight load (design dependent) is ignored for the sake of simplicity. Finally, the wind load is modeled using the ASCE7-22 wind loads and is applied at the edge of the slabs, which is a reasonable assumption considering the cladding. The tower has a fixed boundary condition at the base, which also applies to the column base. The material considered for the outrigger is steel, whereas the slabs, core, and columns are reinforced concrete. The concrete used for the slabs has a compressive strength of $35$ GPa, while the core and columns use concrete with a strength of $60$ GPa.

The tower is divided into four vertical sections, each section having a different core wall thickness and perimeter column size. In other words, the column and core change cross-sections every 21 stories. The outriggers and slabs have a constant thickness of $0.8$ m and $0.2$ m, respectively. The core thicknesses $t_c$ from bottom to top are the following:

$$t_c = \begin{bmatrix} 0.70 & , & 0.50 & , & 0.35 & , & 0.20 \end{bmatrix} \text{ m} \tag{3.2}$$

The core thickness sizing follows a rule-of-thumb that maintains the gravity load stresses under $35\%$ of the available compressive strength. Arguments could be made on this decision, yet this discussion falls outside the scope of the present work. On the other hand, the perimeter columns are square and with cross-section $t_b$ distributed along the 4 sections from bottom to top as:

$$t_b = \begin{bmatrix} 7.29 & , & 3.61 & , & 1.56 & , & 0.56 \end{bmatrix} \text{ m}^2 \tag{3.3}$$

These column sizes are based on the recommendations of Section 22.4.2.2 of ACI318-19 (ACI Committee 318, 2019).

[1]For the sake of simplicity, no superimposed dead load (SDL) or cladding load was considered in this example.

### 3.5.1. Dead and live loads

The gravity loads depend on the materials and building use. The material used for the core and slabs is reinforced concrete, which has a self-weight of $\gamma_c = 24.5$ kN/m$^3$. Also, the building is meant to be an office building with a live load equal to $L = 2.4$ kN/m$^2$, and with a roof live load of $L_r = 0.96$ kN/m$^2$ in accordance with the recommendations of ASCE7-22 (ASCE, 2022). These loads are applied directly on the quadrilateral elements of the slab. Figure 3.16(b) illustrates how the gravitational loads are applied to the structural model.

### 3.5.2. Wind load

The wind load is applied on the exterior nodes of the slabs. The wind load acts as a pressure load on the exterior envelope of the building, which is distributed to the slab edges by the cladding system.

The velocity pressure evaluated at height $z$ above ground $(q_z)$ using Equation 26.10-1.SI from ASCE7-22 (ASCE, 2022), which is reproduced here:

$$q_z = 0.613\, K_z\, K_{zt}\, K_d\, K_e\, V^2 \quad \left(\mathrm{N/m^2}\right)$$

The value of the topographic factor $K_{zt}$ was taken as $K_{zt} = 1$. The directionality factor $K_d$ was taken as $K_d = 0.85$ for buildings where the wind is applied on the *main wind force resisting system* (MWFRS). The ground elevation factor $K_e$ was taken as $K_e = 1$. The exposure for the building was taken as a "category B". Finally, the basic wind speed $V$ was taken as $V = 40$ m/s, which is associated with a 50-year MRI (annual probability of 0.02).

The design wind pressures $p$ acting the MWFRS also requires the values of the gust-effect factor $G$, the external pressure coefficient $C_p$, and the internal pressure coefficient $GCP_i$. To determine the value of the gust-effect factor, we need to know the natural frequency of the building. This is obtained using the (global) stiffness matrix $\mathbf{K}$ and

the mass matrix $\mathbf{M}$ of the structure. The stiffness matrix is already calculated at each optimization iteration. The mass matrix is a requirement that the previous examples did not require, yet it only needs to be calculated once: the outrigger does not contribute towards a design-dependent load (self-weight) and therefore a varying mass matrix. The mass matrix is defined as the seismic weight of the structure, which is taken as $D + 0.25L$, where the dead and live loads are calculated in accordance with Section 3.5.1.

The mass matrix used in this example corresponds to the mass matrix of a flat S4 shell element: a superposition of a Q4D4 (membrane with drilling degrees of freedom) and a P4 (plate) element. The interpolation scheme used in a Q8 element (parent of a Q4D4) is:

$$\mathbf{N} = \begin{bmatrix} N_1 & 0 & N_2 & 0 & \dots & 0 \\ 0 & N_1 & 0 & N_2 & \dots & N_8 \end{bmatrix}$$

The mass matrix $\mathbf{M}_{Q8}$ of the Q8 element is known to be:

$$\mathbf{M}_{\text{Q8}} = \int_{\hat{\Omega}^e} \rho\left(\xi\right) \hat{\mathbf{N}}^T(\xi)\, \hat{\mathbf{N}}\left(\xi\right) \left|\text{det}\mathbf{J}\right| \; \mathrm{d}\hat{\Omega} \tag{3.4}$$

To obtain the mass matrix of a Q4D4 element, we use the transformation matrix $\mathbf{T}_{\text{Q4D4}}$ on $\mathbf{M}_{\text{Q8}}$:

$$\mathbf{M}_{\text{Q4D4}} = \mathbf{T}_{\text{Q4D4}}^T \mathbf{M}_{\text{Q8}} \mathbf{T}_{\text{Q4D4}} \tag{3.5}$$

On the other hand, the interpolation scheme of a P4 element is (Ferreira & Fantuzzi, 2020):

$$\mathbf{N}_w = \begin{bmatrix} N_1 & 0 & 0 & \dots & N_4 & 0 & 0 \end{bmatrix}$$
$$\mathbf{N}_{\theta_x} = \begin{bmatrix} 0 & N_1 & 0 & \dots & 0 & N_8 & 0 \end{bmatrix}$$
$$\mathbf{N}_{\theta_y} = \begin{bmatrix} 0 & 0 & N_1 & \dots & 0 & 0 & N_n \end{bmatrix}$$

, where $\mathbf{N}_w$ corresponds to the shape functions for the transverse displacement $w$ of the plate, and $\mathbf{N}_{\theta_x}$ and $\mathbf{N}_{\theta_y}$ correspond to the shape functions for the rotations $\theta_x$ and $\theta_y$,

respectively. The mass matrix $\mathbf{M}_{\text{P4}}$ can be calculated as:

$$\mathbf{M}_{\text{P4}} = \int_{\hat{\Omega}^e} \rho\left(\xi\right) \hat{\mathbf{N}}^T(\xi) \begin{bmatrix} t & 0 & 0 \\ 0 & \frac{t^3}{12} & 0 \\ 0 & 0 & \frac{t^3}{12} \end{bmatrix} \hat{\mathbf{N}}\left(\xi\right) \left|\text{det}\mathbf{J}\right| \ \mathrm{d}\hat{\Omega} \tag{3.6}$$

where $t$ is the thickness of the plate and $\frac{t^3}{12}$ is the rotary inertia. We then assemble the mass matrix $\mathbf{M}_{\text{S4}}^{\text{(local)}}$ using both mass matrices $\mathbf{M}_{\text{Q4D4}}$ and $\mathbf{M}_{\text{P4}}$ and adding their contributions on the corresponding degree-of-freedom. Finally, a transformation is required to change from the local (flattened) coordinate systems into the structure's global coordinate system:

$$\mathbf{M}_{\text{S4}} = \mathbf{T}_{\text{S4}}^T \, \mathbf{M}_{\text{S4}}^{\text{(local)}} \, \mathbf{T}_{\text{S4}} \tag{3.7}$$

The $\mathbf{M}$ matrix of the building must also consider the contribution of the columns. The mass matrix of columns corresponds to that of an Euler-Bernoulli beam (Craig & Kurdila, 2006). This global mass matrix $\mathbf{M}$ has associated mass for all degrees of freedom of the structure. To solve the eigenvalue problem towards obtaining the natural frequency of the building, we need to obtain $\mathbf{M}$ and $\mathbf{K}$ associated with the unsupported (free) degrees of freedom.

Once the building's natural frequency $n_1$ is known, we can define whether the structure is rigid $(n_1 \geq 1)$ or flexible $(n_1 < 1)$. If the structure is rigid, the value of the gust effect constant $G$ is calculated following Section 26.11.4 of ASCE7-22 (ASCE, 2022), whereas if it is flexible Section 26.11.5 is followed instead. If the structure is flexible, its damping ratio is also necessary to calculate the wind load. Since the structure is made of composite material, the damping ratio ($\zeta$) used in this case is $\zeta = 0.015$ (International Organization for Standardization, 2009). The value of the internal pressure coefficient is taken from Table 26.13-1 in ASCE7-22 (ASCE, 2022), where for a completely enclosed building a value of $GC_{pi} = \pm 0.18$ is taken. The sign depends on the face of the building in which the wind pressure is being calculated. Finally, the values of the external pressure coefficient are taken from Figure 27.3-1 in ASCE7-22 (ASCE, 2022), which also depends on the slenderness of the building in the direction of the wind. When the wind acts in

the $\hat{\mathbf{x}}$ direction, the slenderness is $1.5$, resulting in $C_p = 0.8$ for the windward wall and $C_p = 0.4$ for the leeward wall. On the other hand, for the wind acting in the $\hat{\mathbf{y}}$ direction, the slenderness is $0.67$, so for the windward wall $C_p = 0.8$ and for the leeward wall $C_p = 0.5$. With these parameters, the design wind pressure $p$ for the MWFRS of the building is calculated using Equation 27.3-1 in ASCE7-22 (ASCE, 2022), which is reproduced here:

$$p = q\,GC_p - q_i\,(GC_{pi})$$

The value of $q$ for windward walls is $q_z$, while for leeward walls is $q_h$, which is the velocity pressure evaluated at height $z = h$, where $h$ is the mean roof height of the building.

The wind load, as mentioned before, is applied directly on the perimeter nodes of each slab. The resulting force is obtained assuming the cladding is simply supported between two consecutive slabs. This results in a slightly higher contribution towards to top slab which is most significant near the ground level, because the wind profile varies more near the ground. This process is repeated for every story height and direction in which the wind force is applied. The wind pressure $p$ is applied over the building envelope following cases 1 and 3 of Figure 27.3-8 in ASCE7-22 (ASCE, 2022). These load cases are here illustrated in Figures 3.15(a) and 3.15(b) for completeness.

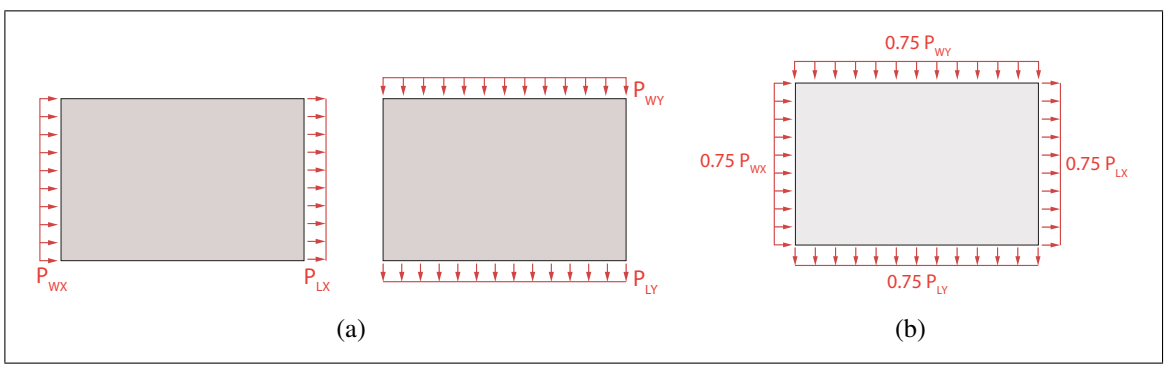


Figure 3.15. Design wind load cases according to ASCE7-22: **(a)** design load case 1; and **(b)** design load case 3.

A floor-plan view of the tower can be seen in Figure 3.16(a), with section cuts A-A and B-B also shown in Figures 3.16(b) and 3.16(c), respectively. These section cuts also illustrate how all loads, gravitational and wind loads, are applied to the structure.

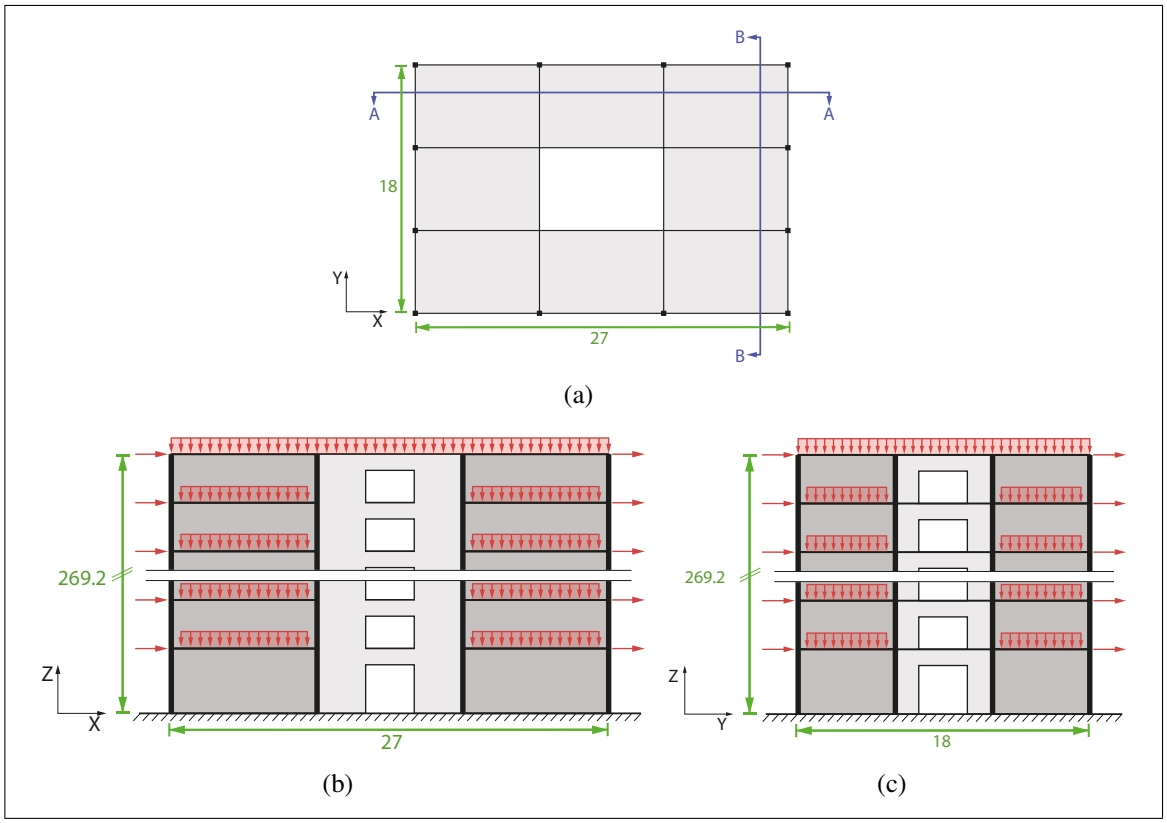


Figure 3.16. High-rise building with outriggers: **(a)** typical floor-plan; **(b)** section along A–A illustrating the application of the gravity and wind loads along the $\hat{\mathbf{x}}$ direction; and **(c)** section along B–B illustrating the application of the gravity and wind loads along the $\hat{\mathbf{y}}$ direction.

The fundamental natural frequency of the building is calculated using Ritz vectors. For this calculation, we use the natural vibration modes as the corresponding Ritz vectors, both, for the $\hat{\mathbf{x}}$ and $\hat{\mathbf{y}}$ directions. Since the matrix $\mathbf{K}$ changes with every iteration, the fundamental natural frequency of the structure also changes. Therefore, the wind loads in the $\hat{\mathbf{x}}$ and $\hat{\mathbf{y}}$ directions should be recalculated in every iteration. That said, the variations on this frequency variation are relatively small and decrease as the solution converges (iterations advance). Because of this, the natural frequency, and therefore the wind load,

is only recalculated at iterations following a Fibonacci sequence (i.e. iterations 1, 2, 3, 5, 8, 13...). This captures the rapid variations on the topology at the initial iterations while saving computations towards the end, but still ensuring an accurate calculation of the wind load throughout the optimization process.

### 3.5.3. Results using compliance

The following results use compliance as the objective function. The design domain with all the possible subdomains is shown in Figure 3.17. The load cases used are taken from Appendix CC of ASCE 7-22 (ASCE, 2022):

(i) $D + 1.0W_x + 0.5L + 0.5L_r$

(ii) $D + 1.0W_y + 0.5L + 0.5L_r$

(iii) $D + 0.75W_x + 0.75W_y + 0.5L + 0.5L_r$

The optimization problem considers all three load cases and follows the procedure for multiple objectives outlined in Section 2.10.

The problem's symmetry was enforced, and the domain was quarterly meshed and replicated throughout all four quadrants. Results for one and two subdomains ($N_0$) were obtained, both associated with different volume fractions. For the case of a single subdomain, the volume fractions are the following: $f_0 = 1 = f_1$ and $f_2 = 3 \cdot 1.2 \cdot N_0/N_f = 0.0179$. On the other hand, the volume fractions for the case of two design subdomains are: $f_0 = 1 = f_1$ and $f_2 = 3 \cdot 1.2 \cdot N_0/N_f = 0.0357$. The density filter has an initial radius $r_{min} = 2.5$, and is reduced through a continuation scheme to a final value of $r_{min} = 0$ (no filter) in the last set of iterations. The penalization $p$ of the element density $\boldsymbol{\rho}$ and the penalization $q$ of the subdomains $\boldsymbol{\mu}$ began both at $1.75$ and $1.75$, respectively. The continuation scheme on $p$ and $q$ took both values to $4.5$. Figure 3.18(a) shows the results for one desired subdomain, whereas Figure 3.18(b) does it for two subdomains.

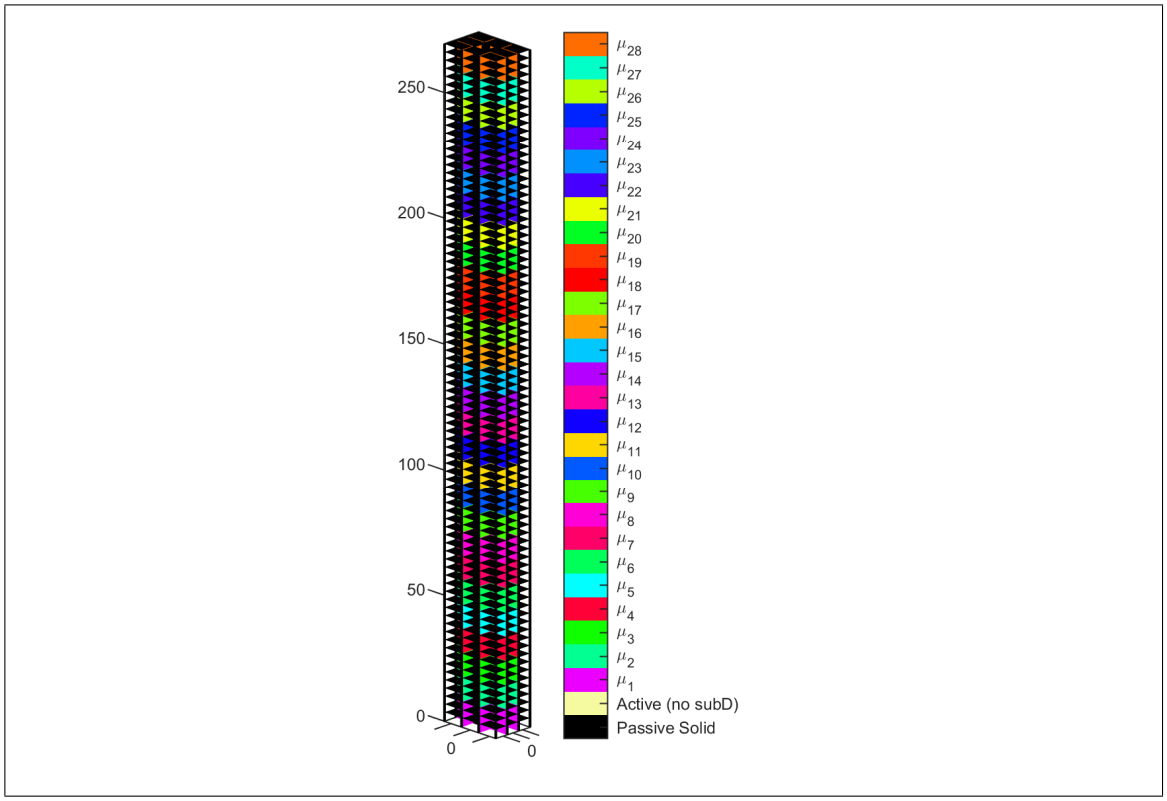


Figure 3.17. Outrigger tower domain.

It can be seen that the proposed method and its implementation succeed in both cases at selecting only the user-specified number of subdomains. For the case of a single subdomain, the chosen one is $\mu_8$; whereas for two subdomains $\mu_8$ and $\mu_9$ were chosen. This last case creates a 6-story high outrigger structure. Direct outriggers connect the core with the perimeter columns using trusses or walls oriented in vertical planes (Choi et al., 2017). Also, both outrigger design types accomplish the same goals: reinforce the perimeter columns and transfer core loads. In addition, a lesser objective of these is to hold the gravity loads of the slab above. From the results, it can be concluded that the outrigger in the $YZ$ plane requires more material than the one in the $XZ$ plane. This is expected since the $YZ$ plane has the lowest aspect ratio, and therefore the fundamental period is in the $\hat{\mathbf{y}}$ direction, resulting in the weakest plane. From a design engineer's point of view: the bulkier topology in the $YZ$ direction suggests that these outrigger trusses could be considered as outrigger walls.

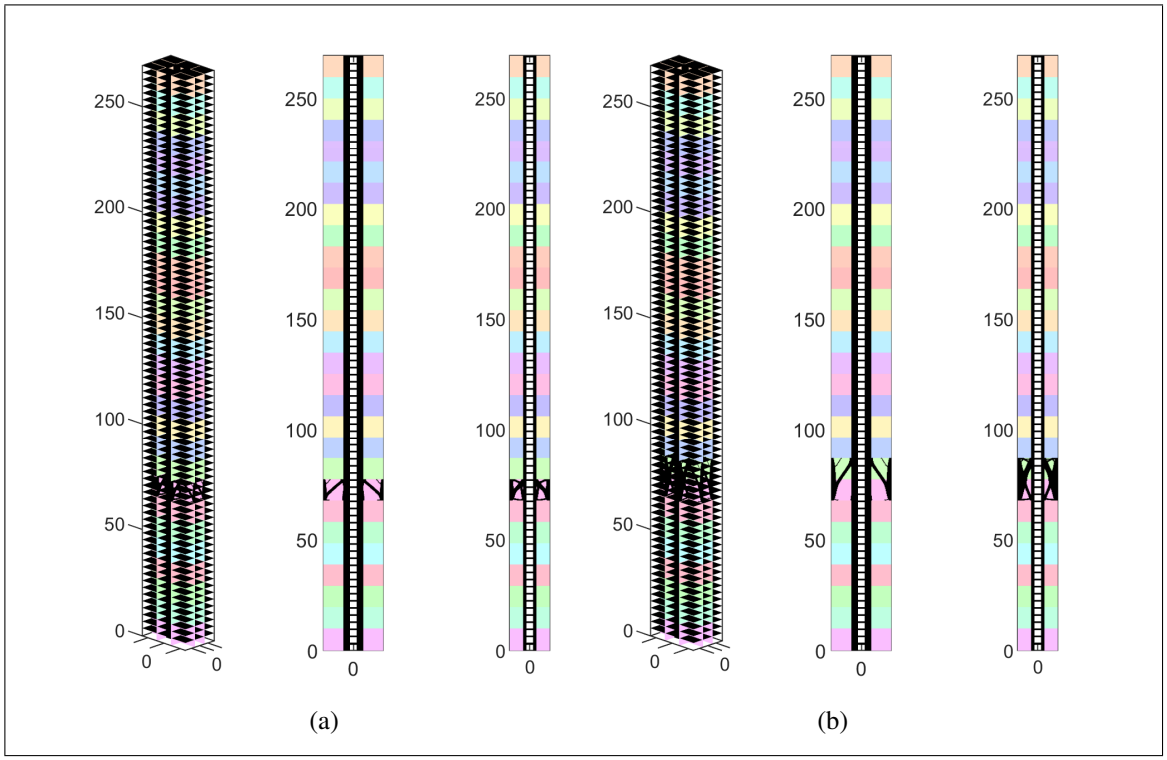


Figure 3.18. Three-dimensional isometric, XZ, and YZ section views of the optimized high-rise building using compliance as the objective function: **(a)** case of a single subdomain (i.e. $N_0 = 1$); and **(b)** case with two available subdomains (i.e. $N_0 = 2$).

Each load case has an associated coefficient $\alpha_i$ which correspond to the objective weights in Equation (2.14) and further described in Section 2.10.1. The final values for each $\alpha_i$ for the case $N_0 = 1$ (single subdomain) are:

$$\begin{bmatrix}\alpha_1 & \alpha_2 & \alpha_3\end{bmatrix} = \begin{bmatrix}0.3057 & 0.5559 & 0.4423\end{bmatrix}$$

On the other hand, the values for $N_0 = 2$ are:

$$\begin{bmatrix}\alpha_1 & \alpha_2 & \alpha_3\end{bmatrix} = \begin{bmatrix}0.3118 & 0.5506 & 0.4426\end{bmatrix}$$

The final values of the constants $\alpha_i$ suggest that the algorithm decided to prioritize load cases 2 and 3, with a bigger emphasis on load case 2. This result is expected because $\hat{\mathbf{y}}$ is the weak direction of the structure which dominates the final design.

### 3.5.4. Results using drift

In this case, the following examples use $J = \mathbf{u}^T \mathbf{D}^T \mathbf{D}\, \mathbf{u}$ as the objective function. Here, matrix $\mathbf{D}$ returns the average of the drift in the $\hat{\mathbf{x}}$ and $\hat{\mathbf{y}}$ directions (as explained in Section 2.11). The tower was run using the same load cases as before, enforcing symmetry, and the same optimization parameters as with compliance.

Results for one and two subdomains ($N_0$) were obtained, both associated with different volume fractions. For the case of a single subdomain, the volume fractions are the following: $f_0 = 1 = f_1$ and $f_2 = 3 \cdot 1.2 \cdot N_0/N_f = 0.0429$. On the other hand, the volume fractions for the case of two design subdomains are: $f_0 = 1 = f_1$ and $f_2 = 3 \cdot 1.2 \cdot N_0/N_f = 0.0857$. The density filter has an initial radius $r_{min} = 0.7$, and is reduced through a continuation scheme to a final value of $r_{min} = 0$ (no filter) in the last set of iterations. The penalization $p$ of the element density $\boldsymbol{\rho}$ and the penalization $q$ of the subdomains $\boldsymbol{\mu}$ began at $1.25$ and $2.25$, respectively. The continuation scheme on $p$ and $q$ took both values to $5.0$ and $4.5$, respectively. Figure 3.19(a) shows the results for one desired subdomain, whereas Figure 3.19(b) does it for two subdomains.

It can be seen that the proposed method and its implementation succeed in both cases at selecting only the user-specified number of subdomains. For the case of a single subdomain, the chosen one is $\mu_{10}$; whereas for two subdomains $\mu_{10}$ and $\mu_{15}$ were chosen.

These results significantly differ from the results using compliance as the objective function. This suggests that the conceptual design of high-rise buildings, more specifically the outrigger location, is likely to be different if the objective is to obtain the stiffest structure (minimal compliance) or minimize the top-floor drift. Additionally, the outrigger topology designs for minimal structural compliance are different than those obtained for minimal drift.

Each load case has an associated coefficient $\alpha_i$ which correspond to the objective weights in Equation (2.14) and further described in Section 2.10.1. The final values for

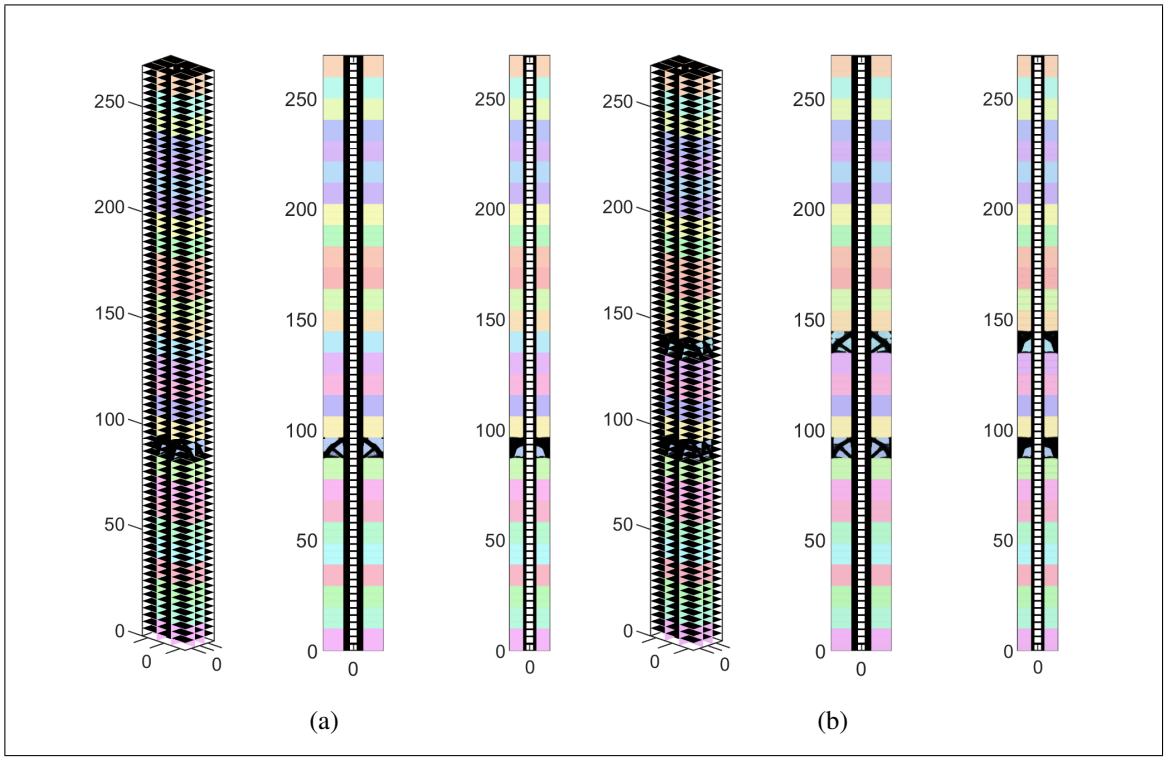


Figure 3.19. Three-dimensional isometric, XZ, and YZ section views of the optimized high-rise building using the top (roof) drift as the objective function: **(a)** case of a single subdomain (i.e. $N_0 = 1$); and **(b)** case with two available subdomains (i.e. $N_0 = 2$).

each $\alpha_i$ for the case $N_0 = 1$ (single subdomain) are:

$$\begin{bmatrix} \alpha_1 & \alpha_2 & \alpha_3 \end{bmatrix} = \begin{bmatrix} 0.0010 & 0.9011 & 0.2159 \end{bmatrix}$$

On the other hand, the values for $N_0 = 2$ are:

$$\begin{bmatrix} \alpha_1 & \alpha_2 & \alpha_3 \end{bmatrix} = \begin{bmatrix} 0.0009 & 0.9022 & 0.2142 \end{bmatrix}$$

Like before (compliance case), the final values of the constants $\alpha_i$ suggest that the algorithm decided to prioritize load cases 2 and 3, with a bigger emphasis on load case 2. This result is expected because $\hat{\mathbf{y}}$ is the weak direction of the structure which dominates the final design.

## 4. CONCLUSIONS

This manuscript develops a formulation for *topology optimization with optimal design subdomain selection* and the examples shown here indicates that the method is successful at its intended purpose. The algorithm can optimally choose and design subdomains in 2D and 3D structures. The user specifies the maximum number of subdomains that can be selected (or used) in the final optimal structure. Additionally, there is a fine control over the amount of material (volume fraction) available for each; the total design domain, the active domain, and the subdomains. This grants the user a flexibility often necessary in real-life optimization problems of this kind. This work considers multiple load cases acting over the structure as is usual in applied real-life problems.

The formulation and algorithm is not free of issues, some of which were highlighted in this manuscript. First, the algorithm is sensitive to the type of penalization used on the subdomains. Some trial-and-error to adjust the penalization parameters (and their continuation scheme) is often necessary. Secondly, the optimal solution depends on the number of subdomains available and thus the user must make an apriori decision. This might not be an issue in applied problems where this matter is well justified, but this decision might trouble more purist researchers in the field with the question of how many selectable subdomains are necessary. Finally, since the optimization is nonlinear, results differ with variations on the continuation schemes for the penalization parameters $p$ and $q$.

## REFERENCES


ACI Committee 318. (2019). *Building Code Requirements for Structural Concrete (ACI 318-19): An ACI Standard ; Commentary on Building Code Requirements for Structural Concrete (ACI 318R-19)*. American Concrete Institute.

Allaire, G., Jouve, F., & Toader, A. (2004, feb). Structural optimization using sensitivity analysis and a level-set method. *Journal of computational physics*, *194*(1), 363–393. doi: 10.1016/j.jcp.2003.09.032

Almeida, S. R. M., Paulino, G. H., & Silva, E. C. N. (2010, jul). Layout and material gradation in topology optimization of functionally graded structures: a global–local approach. *Structural and Multidisciplinary Optimization*, *42*(6), 855–868. doi: 10.1007/s00158-010-0514-x

Andreassen, E., Clausen, A., Schevenels, M., Lazarov, B. S., & Sigmund, O. (2011). Efficient topology optimization in MATLAB using 88 lines of code. *Structural and Multidisciplinary Optimization*, *43*(1), 1–16. doi: 10.1007/s00158-010-0594-7

ASCE. (2022). *(asce 7-22) minimum design loads and associated criteria for buildings and other structures*. American Society of Civil Engineers (ASCE).

Bendsøe, M. P. (1989, August). Optimal shape design as a material distribution problem. *Structural Optimization*, *1*(4), 193–202. doi: 10.1021/jm1000584

Bendsøe, M. P., & Kikuchi, N. (1988, November). Generating optimal topologies in structural design using a homogenization method. *Computer Methods in Applied Mechanics and Engineering*, *71*(2), 197–224. doi: 10.1016/0045-7825(88)90086-2

Bendsøe, M. P., & Sigmund, O. (2003). *Topology optimization: theory, methods and applications* (2nd ed.). Berlin, Germany: Springer.

Bourdin, B. (2001). Filters in topology optimization. *International Journal for Numerical Methods in Engineering*, *50*(9), 2143–2158.

Bruns, T. E., & Tortorelli, D. A. (1998). Topology optimization of geometrically non-linear structures and compliant mechanisms. In $7^{th}$ *aiaa/usaf/nasa/issmo symposium on multidisciplinary analysis and optimization* (pp. 1874–1882). doi: 10.2514/6.1998-4950

Choi, H. S., Ho, G., Joseph, L., & Mathias, N. (2017). *Outrigger Design for High-Rise Buildings* (2nd ed.; J. Gabel, Ed.). Chicago, USA: Council on Tall Buildings and Urban Habitat (CTBUH).

Christensen, P., & Klarbring, A. (2009). *An Introduction to Structural Optimization*. Berlin, Germany: Springer.

Craig, R. R., & Kurdila, A. J. (2006). *Fundamentals of Structural Dynamics* (2nd ed.). Hoboken, USA: Wiley.

Díaz, A., & Sigmund, O. (1995). Checkerboard patterns in layout optimization. *Structural optimization*, *10*(1), 40–45.

Fares, S. S., Coulson, J., & Dinehart, D. W. (2016). *Steel Design Guide 31 – Castellated and Cellular Beam Design*. Chicago, USA: American Institute of Steel Construction (AISC).

Ferreira, A. J. M., & Fantuzzi, N. (2020). *MATLAB Codes for Finite Element Analysis* (2nd ed.). Cham, Switzerland: Springer Nature.

Gain, A. L., & Paulino, G. H. (2012). Phase-field based topology optimization with polygonal elements: A finite volume approach for the evolution equation. *Structural and Multidisciplinary Optimization*, *46*(3), 327–342. doi: 10.1007/s00158-012-0781-9

Guest, J. K., & Zhu, M. (2012, 08). Casting and milling restrictions in topology optimization via projection-based algorithms. In $38^{th}$ *design automation conference* (Vols. 3, Parts

A and B, pp. 913–920). doi: 10.1115/DETC2012-71507

Huang, J., Qin, Q., & Wang, J. (2020). A review of stereolithography: Processes and systems. *Processes*, *8*(9). doi: 10.3390/PR8091138

Huang, X., & Xie, Y. M. (2007). Convergent and mesh-independent solutions for the bi-directional evolutionary structural optimization method. *Finite Elements in Analysis and Design*, *43*(14), 1039–1049. doi: 10.1016/j.finel.2007.06.006

International Organization for Standardization. (2009). *Iso 4354:2009(e) wind actions on structures*. Geneva, Switzerland.

Jog, C. S., & Haber, R. B. (1996, apr). Stability of finite element models for distributed-parameter optimization and topology design. *Computer Methods in Applied Mechanics and Engineering*, *130*(3-4), 203–226. doi: 10.1016/0045-7825(95)00928-0

Kumar, S. (2003). Selective Laser Sintering: A Qualitative and Objective Approach. *Jom*, *55*(10), 43–47. doi: 10.1007/s11837-003-0175-y

Leary, M., Babaee, M., Brandt, M., & Subic, A. (2013, 3). Feasible build orientations for self-supporting fused deposition manufacture: A novel approach to space-filling tesselated geometries. *Advanced Materials Research*, *633*, 148–168. doi: 10.4028/www.scientific.net/AMR.633.148

Leary, M., Merli, L., Torti, F., Mazur, M., & Brandt, M. (2014, 11). Optimal topology for additive manufacture: A method for enabling additive manufacture of support-free optimal structures. *Materials & Design*, *63*, 678–690. doi: 10.1016/j.matdes.2014.06.015

Melchels, F. P., Feijen, J., & Grijpma, D. W. (2010). A review on stereolithography and its applications in biomedical engineering. *Biomaterials*, *31*(24), 6121–6130. doi: 10.1016/j.biomaterials.2010.04.050

Mlejnek, H. P. (1992, 3). Some aspects of the genesis of structures. *Structural Optimization*, *5*, 64–69. doi: 10.1007/BF01744697

Oñate, E. (2013). *Structural Analysis with the Finite Element Method. Volume 2: Beams, Plates and Shells*. Barcelona, Spain: Springer Dordrecht.

Petersson, J. (1999, January). A finite element analysis of optimal variable thickness sheets. *SIAM Journal on Numerical Analysis*, *36*(6), 1759–1778. doi: 10.1137/S0036142996313968

Sigmund, O. (2001). A 99 line topology optimization code written in matlab. *Structural and Multidisciplinary Optimization*, *21*(2), 120–127. doi: 10.1007/s001580050176

Sigmund, O. (2007). Morphology-based black and white filters for topology optimization. *Structural and Multidisciplinary Optimization*, *33*(4-5), 401–424. doi: 10.1007/s00158-006-0087-x

Sigmund, O., & Maute, K. (2013, 12). Topology optimization approaches. *Structural and Multidisciplinary Optimization*, *48*, 1031–1055. doi: 10.1007/s00158-013-0978-6

Stolpe, M., & Svanberg, K. (2001, 4). On the trajectories of the epsilon-relaxation approach for stress-constrained truss topology optimization. *Structural and Multidisciplinary Optimization*, *21*, 140–151. doi: 10.1007/s001580050178

Stromberg, L. L., Beghini, A., Baker, W. F., & Paulino, G. H. (2011). Application of layout and topology optimization using pattern gradation for the conceptual design of buildings. *Structural and Multidisciplinary Optimization*, *43*(2), 165–180. doi: 10.1007/s00158-010-0563-1

Stromberg, L. L., Beghini, A., Baker, W. F., & Paulino, G. H. (2012, apr). Topology optimization for braced frames: Combining continuum and beam/column elements. *Engineering Structures*, *37*, 106–124. doi: 10.1016/j.engstruct.2011.12.034

Suzuki, K., & Kikuchi, N. (1991). A homogenization method for shape and topology optimization. *Computer Methods in Applied Mechanics and Engineering*, *93*(3), 291–318. doi: 10.1016/0045-7825(91)90245-2

Svanberg, K. (1987). The method of moving asymptotes — a new method for structural optimization. *International Journal for Numerical Methods in Engineering*, *24*(2), 359–373. doi: 10.1002/nme.1620240207

Svanberg, K. (accessed December 20, 2022). *MMA and GCMMA – two methods for nonlinear optimization.* Retrieved from `https://people.kth.se/~krille/`

Tang, P. S., & Chang, K. H. (2001). Integration of topology and shape optimization for design of structural components. *Structural and Multidisciplinary Optimization*, *22*(1), 65–82. doi: 10.1007/PL00013282

Taranath, B. S. (2016). *Tall Building Design: Steel, Concrete, and Composite Systems*. Boca Raton, USA: CRC Press.

Tortorelli, D. A., & Michaleris, P. (1994). Design sensitivity analysis: Overview and review. *Inverse Problems in Engineering*, *1*(1), 71–105. doi: 10.1080/174159794088027573

Vatanabe, S. L., Lippi, T. N., Lima, C. R., Paulino, G. H., & Silva, E. C. (2016, 10). Topology optimization with manufacturing constraints: A unified projection-based approach. *Advances in Engineering Software*, *100*, 97–112. doi: 10.1016/j.advengsoft.2016.07.002

Wang, M. Y., Wang, X., & Guo, D. (2003). A level set method for structural topology optimization. *Computer Methods in Applied Mechanics and Engineering*, *192*(1-2), 227–246.

Wang, M. Y., & Zhou, S. (2004). Phase field: A variational method for structural topology optimization. *CMES – Computer Modeling in Engineering and Sciences*, *6*(6), 547–566.

Xie, Y. M., & Steven, G. P. (1997). *Evolutionary Structural Optimization*. London, UK: Springer.

Zegard, T., Baker, W. F., Mazurek, A., & Paulino, G. H. (2014, sep). Geometrical Aspects of Lateral Bracing Systems: Where Should the Optimal Bracing Point Be? *Journal of Structural Engineering*, *140*(9), 04014063. doi: 10.1061/(ASCE)ST.1943-541X.0000956

Zegard, T., & Paulino, G. H. (2016). Bridging topology optimization and additive manufacturing. *Structural and Multidisciplinary Optimization*, *53*(1), 175–192. doi: 10.1007/s00158-015-1274-4

Zhou, M., & Rozvany, G. (1991, 8). The COC algorithm, part II: Topological, geometrical and generalized shape optimization. *Computer Methods in Applied Mechanics and Engineering*, *89*, 309–336. doi: 10.1016/0045-7825(91)90046-9

# APPENDIX

# A. NOMENCLATURE

| | |
|---|---|
| $E^{(i)}$ | Elastic modulus of the $i$-th element |
| $E_{min}$ | Elastic modulus associated with Ersatz material |
| $E_0$ | Elastic modulus of the solid phase |
| $\mathbf{f}_i$ | Nodal force vector of the $i$-th load case |
| $f_0$ | Volume fraction of complete domain |
| $f_1$ | Volume fraction of complete domain minus subdomains |
| $f_2$ | Volume fraction of subdomains |
| $\mathbf{H}$ | Filter matrix |
| $J_i$ | Objective function of the $i$-th load case |
| $\mathbf{K}_0^{(i)}$ | Stiffness matrix of the $i$-th element using $E = 1$ |
| $\mathbf{K}$ | Global stiffness matrix |
| $N_{\text{dof}}$ | Number of degrees of freedom |
| $N$ | Number of elements in the complete domain |
| $N_s$ | Number of selectable subdomains |
| $N_0$ | Maximum number of design subdomains |
| $N_1$ | Number of elements in the complete domain minus the subdomains |
| $N_2$ | Number of elements in subdomains |
| $p$ | Density penalization parameter |
| $q$ | Subdomain penalization parameter |
| $r_{min}$ | Filter size |
| $\mathbf{u}_i$ | Nodal displacement vector of the $i$-th load case |
| $v_0$ | Volume of complete domain |
| $v_1$ | Volume of complete domain minus the subdomains |
| $v_2$ | Volume of subdomains |
| $\mathbf{x}$ | Vector of the $N$ element-wise design variables |

$\alpha_i$ Contribution constant of $i$-th load case

$\beta$ P-norm constant

$\varepsilon$ Relaxation parameter

$\boldsymbol{\lambda}$ Adjoint vector

$\boldsymbol{\mu}$ Vector of $N_s$ subdomains design variables

$\boldsymbol{\rho}$ Vector of the $N$ element-wise densities